Draft version January 16, 2017
Typeset using LaTeX default style in AASTeX61

A LARGE CATALOG OF HOMOGENEOUS ULTRA-VIOLET/OPTICAL GRB AFTERGLOWS: TEMPORAL AND SPECTRAL EVOLUTION

Peter W. A. Roming,[1,2,3] T. Scott Koch,[4] Samantha R. Oates,[5] Blair L. Porterfield,[6] Amanda J. Bayless,[1,3] Alice A. Breeveld,[5] Caryl Gronwall,[2,7] N. P. M. Kuin,[5] Mat J. Page,[5] Massimiliano de Pasquale,[5] Michael H. Siegel,[2] Craig A. Swenson,[8] and Jennifer M. Tobler[9]

[1] *Southwest Research Institute*
Space Science & Engineering Division
6220 Culebra Road
San Antonio, TX 78238-5166, USA
[2] *The Pennsylvania State University*
Department of Astronomy & Astrophysics
525 Davey Lab
University Park, PA 16802, USA
[3] *University of Texas at San Antonio*
Department of Physics & Astronomy
1 UTSA Circle
San Antonio, TX 78249, USA
[4] *The Pennsylvania State University*
Classroom & Lab Computing
101E Computer Building
University Park, PA 16802, USA
[5] *Mullard Space Science Laboratory*
University College London
Holmbury St. Mary
Dorking, Surrey RH5 6NT, UK
[6] *Space Telescope Science Institute*
3700 San Martin Drive
Baltimore, MD 21218, USA
[7] *The Pennsylvania State University*
Institute for Gravitation and the Cosmos
University Park, PA 16802, USA
[8] *Science Systems and Applications, Inc.*
10210 Greenbelt Road
Lanham, MD 20706, USA
[9] *University of North Dakota*
Department of Space Studies
4149 University Avenue
Grand Forks, ND 58202-9008, USA

(Received May 6, 2016; Revised December 12, 2016; Accepted December 21, 2016)

Submitted to ApJS

ABSTRACT

We present the second *Swift* Ultra-Violet/Optical Telescope (UVOT) gamma-ray burst (GRB) afterglow catalog, greatly expanding on the first *Swift* UVOT GRB afterglow catalog. The second catalog is constructed from a database containing over 120,000 independent UVOT observations of 538 GRBs first detected by *Swift*, the *High Energy Transient Explorer 2* (HETE2), the *INTErnational Gamma-Ray Astrophysics Laboratory* (INTEGRAL), the Interplanetary Network (IPN), *Fermi*, and *Astro-rivelatore Gamma a Immagini Leggero* (AGILE). The catalog covers GRBs discov-

Corresponding author: Pete Roming
proming@swri.edu

ered from 2005 Jan 17 to 2010 Dec 25. Using photometric information in three UV bands, three optical bands, and a '*white*' or open filter, the data are optimally co-added to maximize the number of detections and normalized to one band to provide a detailed light curve. The catalog provides positional, temporal, and photometric information for each burst, as well as *Swift* Burst Alert Telescope (BAT) and X-Ray Telescope (XRT) GRB parameters. Temporal slopes are provided for each UVOT filter. The temporal slope per filter of almost half the GRBs are fit with a single power-law, but one to three breaks are required in the remaining bursts. Morphological comparisons with the X-ray reveal that $\sim$ 75% of the UVOT light curves are similar to one of the four morphologies identified by Evans et al. (2009). The remaining $\sim$ 25% have a newly identified morphology. For many bursts, redshift and extinction corrected UV/optical spectral slopes are also provided at 2×10^3, 2×10^4, and 2×10^5 seconds.

Keywords: catalogs — gamma-rays: bursts

1. INTRODUCTION

The Ultraviolet/Optical Telescope (UVOT; Roming et al. 2000, 2004, 2005) on board the *Swift* observatory (Gehrels et al. 2004), is designed to rapidly follow-up gamma-ray burst (GRB) afterglows in the $170 - 800$ nm range. UVOT observations of GRB afterglows were first cataloged by Roming et al. (2009, hereafter Paper1) and includes 229 bursts discovered between 2005 January 17 and 2007 June 16. These bursts were primarily discovered by *Swift* but also include GRBs discovered by the *High Energy Transient Explorer 2* (HETE2; Ricker 1997), *INTErnational Gamma-Ray Astrophysics Laboratory* (INTEGRAL), and Interplanetary Network (IPN; Hurley et al. 2005). In Paper1, positional, temporal, and photometric information is provided for each GRB afterglow, as well as filter-dependent light curves which are fit with a single power-law.

In this paper we describe the second *Swift* UVOT GRB afterglow catalog and corresponding databases, which contain information on bursts observed during the first six years of UVOT operations (2005-2010). This catalog more than doubles the number of observed GRBs and also includes UVOT observations of *Fermi* Large Area Telescope (LAT; Atwood et al. 2009) and *Astro-rivelatore Gamma a Immagini Leggero* (AGILE; Tavani et al. 2009) discovered GRBs. The catalog and databases include much of the same type of information provided in Paper1 but also include important additions: data is optimally co-added (Morgan et al. 2008, hereafter M08) to increase the number of detections, optimally co-added data is normalized to a given bandpass, and normalized data are fit with single and broken power-laws. Additionally, redshift and extinction corrected spectral slopes and filter dependent temporal slopes are provided.

In Section 2 we present the observations made by the UVOT. In Section 3 we describe the construction of the image/event and normalized optimally co-added databases and the resulting GRB catalog. In Section 4 we describe the databases and catalog. In Section 5 we provide a summary of the catalog and in Section 6 discuss future work. The databases and catalogs are provided in electronic format as part of this paper and are also available at the Barbara A. Mikulski Archive for Space Telescopes (MAST)[1] and *Swift*[2] websites.

2. OBSERVATIONS

The UVOT utilizes seven broadband filters during the observation of GRBs: uvw2 ($\lambda_c = 193$ nm), uvm2 ($\lambda_c = 225$ nm), uvw1 ($\lambda_c = 260$ nm), u ($\lambda_c = 346$ nm), b ($\lambda_c = 439$ nm), v ($\lambda_c = 547$ nm), and a clear-filter (Roming et al. 2005; Poole et al. 2008). Data in each filter are collected in either image or event mode. In image mode, individual photons are collected, aspect corrected, and added to an onboard image buffer. At the conclusion of an exposure, images are packaged and sent to the spacecraft awaiting transfer to the ground. In event mode, individual photons are collected, time tagged, and sent to the ground where they are converted to event lists and aspect corrected sky images. The event data is used to create high time resolution (~ 11 ms) photometry of bright bursts while image data is used for fainter sources. A more complete description of the filters, image acquisition, and observing sequences can be found in Paper1.

This catalog includes 626 bursts first detected by the *Swift* Burst Alert Telescope (BAT; Barthelmy et al. 2005), HETE2, INTEGRAL, IPN, LAT, and AGILE during the period from 2005 Jan 17 to 2010 Dec 25. A total of 538 of the 626 bursts were observed (but not necessarily detected) by the UVOT representing 86% of the cataloged bursts. Bursts detected by BAT but not observed by UVOT were either too close in angular distance to a bright ($\lesssim 6$ mag) source (including the Sun and Moon), or occurred during UVOT engineering operations.

Hereafter, we adopt the notation $F(\nu, t) \propto t^{\alpha}\nu^{\beta}$ for the afterglow flux density as a function of time, where ν is the frequency of the observed flux density, t is the time post trigger, β is the spectral index which is related to the photon index Γ ($\beta = \Gamma - 1$) , and α is the temporal decay slope.

3. CONSTRUCTION OF THE DATA PRODUCTS

To provide context for understanding the work described herein, we define the following: image pipeline, event pipeline, databases, and catalog. The image pipeline is an IDL-based program that incorporates the UVOT tool, `uvotsource`[3], and is used to perform photometry on Level-1 images. The event pipeline is a collection of tools used to perform fine aspect corrections on UVOT event data and photometric measurements on the resulting event lists; photometry is performed with `uvotevtlc`. The event pipeline software is described in detail elsewhere (Oates et al.

[1] https://archive.stsci.edu/prepds/uvotgrb/

[2] http://swift.gsfc.nasa.gov/results/uvot_grbcat2/

[3] http://heasarc.nasa.gov/ftools/caldb/help/uvotsource.html

2009). The databases are a repository for all photometric measurements made by the photometry pipeline. There are two databases: the image/event database that is the result of processing the raw UVOT data, and the normalized optimally co-added (NOC) database that is the final product used to produce the NOC light curves. The catalog is a compilation of the top-level data derived from the image/event and NOC databases, and other sources such as the BAT catalog (Sakamoto et al. 2008, 2011), the *Swift* GRB archive[4] (SGA), and the Gamma-ray burst Coordinate Network (GCN; Barthelmy et al. 1995, 1998) circulars. As such, this catalog provides the primary characteristics for each burst.

3.1. *Image/Event Database Construction*

The image/event database was constructed using the image and event pipelines which are essentially the same as those described in Sections 3.1 and 3.2 of Paper1. Differences are noted below.

To ensure that all images and exposure maps benefited from consistent and up-to-date calibrations, the *Swift* Data Center (SDC) reprocessed images taken before GRB 070621. This reprocessing was necessary due to the fact that earlier versions of the processing pipeline did not take advantage of essential lessons learned from the first years of operations. Images for subsequent bursts were taken directly from the *Swift* archive. The FTOOL `uvotskycorr` was manually run on a small number of archive images to improve the aspect solution. In Paper1, we reported the position of potentially contaminating sources. This has been dropped from the current version of the database since its primary purpose is already accounted for in a quality flag.

For event lists, all available event data (including settling exposures) from the first observation segment, which can span more than one orbit, was extracted; in Paper1, we only considered event data taken in the *v*- and *white*-filters in the first orbit. We note that for the earliest settling exposures ($\lesssim 4$ s) the cathode is still warming up, therefore these exposures can produce erroneous values. All settling exposures in these databases are marked with a quality flag.

Both image and event pipelines utilized HEADAS Version 6.10 and the 2011 January 31 UVOT CALDB. In Paper1, we provided only $3''.0$ radius apertures that were used for aperture photometry. In this version we provide both $3''.0$ and $5''.0$ radius photometry apertures in the image and event pipelines. Upper limits were reported for sources $< 2\sigma$. Here we use 2σ instead of 3σ (as in Paper1) since the position of the burst is often known to the arcsecond-level.

To determine the fraction of false positives (f_{FP}) we use Equation 1, where N_{ND} is the number of non-detections ($< 2\sigma$) in the catalog (98,601 and 98,689 for the $3''.0$ and $5''.0$ databases, respectively), $Q(2)$ is the Q-function[5] at two standard deviations, and M is the number of observations (119,598 and 120,217).

$$f_{FP} = N_{ND} Q(2)(1 - Q(2))^{-1} M^{-1} \quad (1)$$

We conservatively estimate that the fraction of false positives is 1.92% and 1.91% for the $3''.0$ and $5''.0$ databases, respectively.

3.2. *Normalized Optimally Co-added Database Construction*

The NOC Database was created through a five step process: initial optimal co-addition of the data, preliminary fits to the light curves, rerunning of the optimal co-addition, refitting of the light curves, and normalization of the color light curves to a single filter. Optimal co-addition is one of the fundamental differences between this work and that presented in Paper1.

The first step was to perform optimal co-addition on each burst in the $5''.0$ image/event database for each filter. Optimal co-addition uses the α of a GRB to "optimally weight each exposure during image summation to maximize the signal-to-noise of the final co-added image" (M08). This initial step recovers a greater number of individual detections in each filter with which to generate light curves. Our method differs slightly from the one provided by the FTOOL `uvotoptsum` since `uvotoptsum` is optimized for individual detections whereas our code is optimized for producing detailed light curves. M08 have shown that using an α within ± 0.5 of the actual GRB α during optimal co-addition provides for a more significant detection than an unweighted co-addition technique; therefore, during the initial optimal co-addition process, we used a "canonical" α of 0.88, an average decay value determined from a sample of light curves for > 500 s after the trigger (Oates et al. 2009). From the optimally co-added data we produced detailed light curves for each burst in each filter.

[4] http://swift.gsfc.nasa.gov/archive/grb_table/

[5] See http://cnx.org/contents/hDU5uzaA@2/The-Q-function for a description of the Q-function.

We then fit each segment, or data points between break times, of the light curve with a single power law varying the temporal slope each time. Our fitting routine is centered around the IDL-based program `mpfit` (Markwardt 2009). For each α, a model fit is produced, compared to the data, and an overall χ^2_{Red} for the entire light curve is calculated. For purposes of this catalog, we assume that the cooling frequency (ν_c) has not, or has already, passed through the UVOT bandpass for all bursts. Confirmation of this assumption will be provided in a forthcoming publication. Based on this assumption, for each segment of the burst and a given α, the average χ^2_{Red} for all filters is calculated. The α with an average χ^2_{Red} that most closely approaches unity is the temporal slope used for the given segment in the remaining steps.

With newly determined temporal slopes for each burst, optimal co-addition was rerun on each burst in the image/event database. The newly produced light curves were then refitted as described previously (e.g. Figure 1). All color light curves for each burst were then normalized to a given band (typically v-band) and then fit with a single, broken, or multiply-broken power law (e.g. Figure 1), as described in Racusin et al. (2009).

3.3. *Quality Control*

As in Paper1, we compare a sample of the resultant light curves with those published in the literature to check for consistency: GRBs 050525A (Blustin et al. 2006), 050603 (Grupe et al. 2006), 050730 (Perri et al. 2007), 050801 (De Pasquale et al. 2007), 050802 (Oates et al. 2007), 060124 (Romano et al. 2006), 060313 (Roming et al. 2006a), 060729 (Grupe et al. 2007), 061007 (Schady et al. 2007), 070125 (Updike et al. 2008), 080319B (Racusin et al. 2008), 080810 (Page et al. 2009), 081008 (Yuan et al. 2010), 081203A (Kuin et al. 2009), 090426 (Xin et al. 2011), 090510 (De Pasquale et al. 2010), and 090902B (Pandey et al. 2010). For each of these bursts, we look for at least three events with comparable exposure times at similar epochs while keeping the normalized and published filters the same whenever possible. Based on these criteria, we compare the magnitudes, fluxes, or count rates to determine if they are consistent with each other, within the errors. We note that some values are visually extracted from the literature for comparison as there are no tabular values available. Our resultant light curves are found to be consistent with the published values.

3.4. *GRB Catalog Construction*

The UVOT GRB Catalog was constructed by combining information from various databases and catalogs. The filter, magnitude, and flux[6] of the first and peak detections, along with the start times of these events, were taken from the image/event database for each burst. Temporal slopes in each filter for each burst were derived from the NOC light curves. From these temporal slopes, dust extinction and redshift corrected fluxes in each filter were computed at 2×10^3 s, 2×10^4 s, and 2×10^5 s and spectral slopes were determined. These times were chosen so as to be after the period of greatest afterglow variation (500 s; Oates et al. 2009) and to span two decades in time. Details of the spectral slope fitting are provided in Table 6-Column 332.

Additional information for the catalog was gleaned from the UVOT data, SGA, or the literature. A reference to the best reported burst position is provided. Also included is a flag indicating which observatory discovered each burst. The burst trigger time, T_{90}, BAT fluence, BAT peak photon flux, BAT photon index, *Swift* X-Ray Telescope (XRT; Burrows et al. 2005) flux at various epochs, XRT temporal and spectral indices, and the HI column density along the line of sight are from the SGA and are provided in the catalog for each burst.

4. DATABASE AND CATALOG FORMATS

The image/event databases, the NOC database, and the *Swift* UVOT GRB Catalog can be found in their entirety in the electronic version of this paper and at the MAST and *Swift* websites. Sample columns and rows are provided in Table 1, Table 2, and Table 3, respectively. The databases and catalog are available in binary FITS format and are 46.6 MB, 46.8 MB, 1.4 MB, and 1.0 MB in size for the $3''.0$ image/event, $5''.0$ image/event, and NOC databases, and the catalog, respectively. The $3''.0$ image/event database contains 81 columns and $119,598$ rows, the $5''.0$ image/event database contains 81 columns and $120,217$ rows, the NOC database contains 20 columns and 13,597 rows, and the GRB catalog contains 349 columns and 626 rows. A description of each column in the image/event databases, NOC database, and the *Swift* UVOT burst catalog can be found in Table 4, Table 5, and Table 6, respectively.

[6] We use the standard flux conversion factors from the CALDB for a GRB.

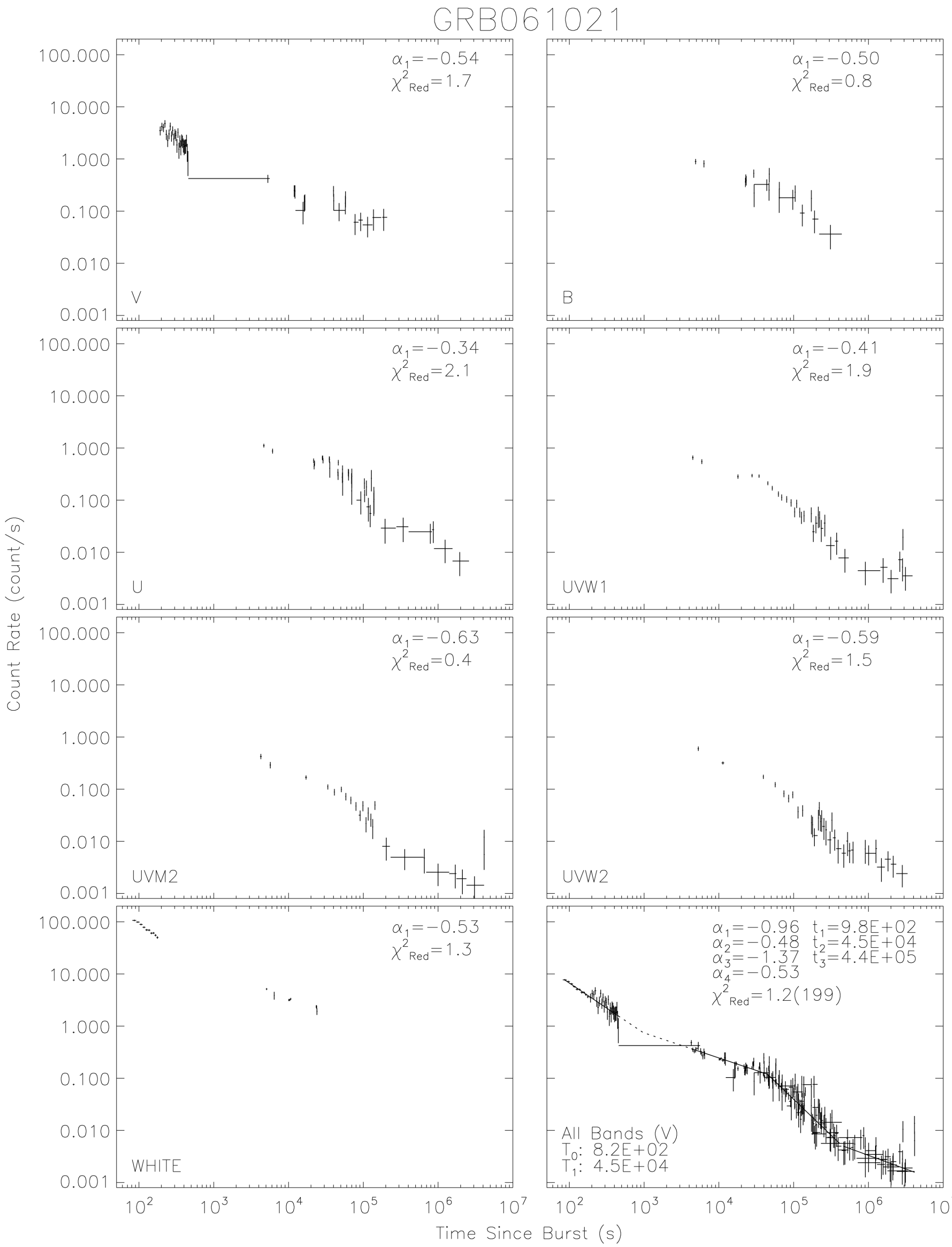

Figure 1. An example of optimally co-added light curves in each UVOT filter (as marked in the lower left of each panel) for a given GRB. The lowest right panel is the normalized light curve (normalized to the filter over the temporal range T_0 to T_1 as specified in the lower left of the panel) with the given temporal slopes and break times provided in the upper left of the panel.

Table 1. Selected sample from the 3.″0 *Swift*/UVOT Image/Event Database

OBJECT	TSTART	EXPOSURE	FILTER	RAW_TOT_CNTS	MAG
GRB050525	138672355.3	9.62	UVM2	94.1	14.13
GRB050525	138672369.5	9.60	UVW1	188.2	13.99
GRB050525	138672383.1	9.61	U	309.7	14.21
GRB050525	138672397.2	9.61	B	271.0	15.19
GRB050525	138672412.4	9.61	UVW2	79.0	14.84
GRB050525	138672426.1	9.60	V	116.1	15.02

Note—This table and the corresponding 5.″0 *Swift*/UVOT Image/Event Database is available in its entirety in FITS format in the online journal, MAST, and the *Swift* website. A portion is shown here for guidance regarding its form and content.

Table 2. Selected sample from the *Swift*/UVOT Normalized Co-added Database

OBJECT	FILTER	TSTART	EXPOSURE	MAG	SIGMA	ALPHA
GRB050525	V	688.45	9.61	15.47	4.6	-1.0000
GRB050525	UVM2	702.64	9.60	15.69	7.3	-1.0000
GRB050525	UVW1	716.25	9.60	16.02	10.6	-1.0000
GRB050525	U	730.44	9.61	15.82	10.4	-1.0000
GRB050525	B	745.58	9.60	15.51	6.0	-1.0000
GRB050525	UVW2	759.22	9.60	16.44	5.7	-1.0000

Note—This table is available in its entirety in FITS format in the online journal, MAST, and the *Swift* website. A portion is shown here for guidance regarding its form and content.

Table 3. Selected sample from the *Swift*/UVOT GRB Catalog

OBJECT	RA	DEC	POS_ERR	POS_REF	DISC_BY
GRB050318	49.712529	-46.395496	0.60	SGA	0
GRB050319	154.199625	43.548290	0.50	SGA	0
GRB050326	6.946208	-71.370583	2.40	SGA	0
GRB050401	247.870083	2.187453	0.50	GCN3187	0
GRB050406	34.467500	-50.187725	0.60	SGA	0
GRB050408	180.572167	10.852778	1.00	GCN3192	1
GRB050410	89.808792	79.603444	1.70	SGA	0
GRB050412	181.104417	-1.201000	0.50	GCN3255	0
GRB050416A	188.477500	21.057415	1.00	SGA	0

NOTE—This table is available in its entirety in FITS format in the online journal, MAST, and the *Swift* website. A portion is shown here for guidance regarding its form and content.

Table 4. Description of *Swift*/UVOT Image and Event Databases

Column	Label	Description
1	OBJECT	Object identification. The format is GRB$yymmddX$, where yy is the last two digits of the year of the burst, mm is the month, dd is the day (in UTC), and X is used to represent the first, second, third, etc., burst occurring on a given day by the letters 'A', 'B', 'C', etc. In some cases the 'A' is not displayed.
2	RA	J2000.0 right ascension in decimal degrees.
3	DEC	J2000.0 declination in decimal degrees.
4	POS_ERR	Positional uncertainty in arcseconds.
5	TRIGTIME	Time of burst trigger as measured in *Swift* mission elapsed time (MET). MET is measured in seconds and starts on 2001 January 1, 00:00:00.000 (UTC). *Swift* launch MET is 122668545.865 (2004 November 20, 18:35:45.865 UTC).
6	TRIG_UT	Time of burst trigger as measured in UTC (e.g. 2005-017-12:52:36). Due to an error in the processing code some UTC times (TRIG_UT) have not been corrected for clock drift, therefore, these values should be treated with caution. MET (TRIGTIME) is not affected by clock drift.
7	TSTART	MET start time of the exposure.
8	TSTOP	MET stop time of the exposure.
9	TELAPSE	TSTOP - TSTART in seconds.
10	TIME	TSTART + TELAPSE/2 (see columns 7 and 9).
11	TSINCE_BUR	Time since burst trigger in seconds (TSTART - TRIGTIME).
12	EXPOSURE	Corrected exposure time in seconds. Corrections include: detector dead time, time lost when the spacecraft drift is large enough that event data is lost, time lost when the UVOT Digital Processing Unit buffers fill due to high count rates, and time lost due to exposures in the UVOT blocked filter.
13	FILTER	UVOT filter used for exposure (uvw2, uvm2, uvw1, u, b, v, and *white*).
14	BINNING	Binning factor ($1 = 1 \times 1$ and $2 = 2 \times 2$ sq-pixel binning) for $0\farcs5$ pixels.
15	APERTURE	Photometric aperture radius in arcseconds.
16	SRC_AREA	Area of source aperture in square arcseconds, computed by multiplying the number of pixels found by XIMAGE within the source radius by the area of each pixel. This value can differ from the specified area πr^2 by up to 2% because XIMAGE selects whole pixels within the source radius. This approach produces an area slightly larger or smaller than πr^2. Simulations reveal that the 1σ difference between the exact and XIMAGE areas are 1.0% and 1.5% for a 10 and 6 pixel radius, respectively. The error in photometry is much less than these area fluctuations because source counts are concentrated in the center of the aperture and the aperture correction uses

Table 4 continued on next page

Table 4 *(continued)*

Column	Label	Description
		the radius corresponding to the XIMAGE area.
17	BKG_AREA	Area, in square arcseconds, of the background region. It is calculated by taking the number of pixels in the background annulus and multiplying by the area of each pixel. Masked regions are excluded therefore only net pixels are included. This differs slightly from the exact area $\pi(r_o - r_i)^2$, but we are only interested in the background surface brightness, so the difference is not significant.
18	PLATE_SCALE	Image plate scale in arcseconds per pixel. Error in the mean plate scale is $\pm0\farcs0005$ pixel^{-1}.
19	RAW_TOT_CNTS	Total number of counts measured within the source region.
20	RAW_TOT_CNTS_ERR	Binomial error in RAW_TOT_CNTS. The binomial error is given by (RAW_TOT_CNTS)$^{1/2}$ $*$ ((NFRAME − RAW_TOT_CNTS)/NFRAME)$^{1/2}$ where NFRAME = TELAPSE / FRAMTIME and FRAMTIME = 0.011032 s for the full FoV. NFRAME is the number of CCD frames (typically one every $\sim$ 11 ms). A discussion of the measurement errors in the UVOT can be found in Kuin & Rosen (2008).
21	RAW_BKG_CNTS	Total number of counts measured in the background annulus.
22	RAW_BKG_CNTS_ERR	Binomial error in RAW_BKG_CNTS. The binomial error is given by (RAW_BKG_CNTS)$^{1/2}$ $*$ ((NFRAME − EFF_BKG_CNTS)/NFRAME)$^{1/2}$ where EFF_BKG_CNTS = RAW_BKG_CNTS * 80 / BKG_AREA. The effective counts in the background (EFF_BKG_CNTS) is calculated because the background area is larger than the coincidence region. The value 80 is the area (in square arcseconds) of our circular aperture with a radius of 5″.
23	RAW_STD_CNTS	Total number of counts measured within the standard 5″ aperture. This constant value is based on the size of the current calibration aperture.
24	RAW_STD_CNTS_ERR	Binomial error associated with RAW_STD_CNTS.
25	RAW_TOT_RATE	Total measured count rate, in counts per second, in the source region. Calculated using RAW_TOT_CNTS / EXPOSURE.
26	RAW_TOT_RATE_ERR	RAW_TOT_CNTS_ERR / EXPOSURE.
27	RAW_BKG_RATE	Total measured count rate, in counts per second per square arcsecond, in the background region. Calculated using RAW_BKG_CNTS / EXPOSURE / BKG_AREA.
28	RAW_BKG_RATE_ERR	RAW_BKG_CNTS_ERR / EXPOSURE / BKG_AREA.
29	RAW_STD_RATE	Total measured count rate, in counts per second, in the coincidence loss region. Calculated using RAW_STD_CNTS / EXPOSURE.
30	RAW_STD_RATE_ERR	RAW_STD_CNTS_ERR / EXPOSURE.
31	COI_STD_FACTOR	Coincidence-loss correction factor for the coincidence-loss region. This is

Table 4 continued on next page

Table 4 *(continued)*

Column	Label	Description
		calculated as follows. First, the COI_STD_RATE (which is not recorded) is calculated using the theoretical coincidence loss formula and the polynomial correction to RAW_STD_RATE (see eq. 1-3 in Poole et al. 2008). The value COI_STD_FACTOR is then the ratio COI_STD_RATE / RAW_STD_RATE.
32	COI_STD_FACTOR_ERR	Uncertainty in the coincidence correction (see eq. 4 in Poole et al. 2008).
33	COI_BKG_FACTOR	Coincidence-loss correction factor for the background region.
34	COI_BKG_FACTOR_ERR	Uncertainty in the coincidence correction of the background counts within the source aperture.
35	COI_TOT_RATE	Coincidence-loss corrected raw count rate, in counts per second, in the source region. Calculated using RAW_TOT_RATE * COI_STD_FACTOR.
36	COI_TOT_RATE_ERR	Error in the COI_TOT_RATE. RAW_TOT_RATE_ERR * COI_STD_FACTOR.
37	COI_BKG_RATE	Coincidence-loss corrected background surface count rate, in counts per second per square arcsecond. Calculated using RAW_BKG_RATE * COI_BKG_FACTOR.
38	COI_BKG_RATE_ERR	Error in coincidence corrected background surface brightness. Calculated using RAW_BKG_RATE_ERR * COI_BKG_FACTOR.
39	COI_SRC_RATE	Coincidence corrected net count rate, in counts per second. Calculated using COI_TOT_RATE - COI_BKG_RATE * SRC_AREA.
40	COI_SRC_RATE_ERR	Error in the coincidence corrected net count rate. Errors in the source rate and the background rate are added in quadrature: $(\mathrm{COI\_TOT\_RATE\_ERR}^2 + (\mathrm{COI\_BKG\_RATE\_ERR} * \mathrm{SRC\_AREA})^2)^{1/2}$
41	AP_FACTOR	Aperture correction for going from a $3''$ radius to a $5''$ radius aperture for the v filter. This is computed using the PSF stored in the CALDB by `uvotapercorr`. This is always set to 1.0 unless the `CURVEOFGROWTH` method is used. The source radius is defined to be $(\mathrm{SRC\_AREA}/\pi)^{1/2}$, so that one uses an effective source radius to the actual pixel area used by XIMAGE.
42	AP_FACTOR_ERR	The 1σ error in AP_FACTOR. AP_FACTOR_ERR = AP_COI_SRC_RATE_ERR / COI_SRC_RATE_ERR.
43	AP_COI_SRC_RATE	Aperture and coincidence loss corrected count rate used to derive the flux and magnitudes for the NOC database. Calculated using AP_FACTOR * COI_SRC_RATE.
44	AP_COI_SRC_RATE_ERR	Error on the count rate. Calculated using $(\mathrm{COI\_SRC\_RATE\_ERR}^2 + (\mathrm{fwhmsig} * \mathrm{COI\_SRC\_RATE})^2)^{1/2}$ where the "fwhmsig" parameter is the fractional RMS variation of the PSF which is set to $3''$. This variation is propagated through the uncertainty calculation, and is added in quadrature to the corrected measurement uncertainty.

Table 4 continued on next page

Table 4 *(continued)*

Column	Label	Description
45	LSS_FACTOR	Large-scale sensitivity factor to be applied to AP_COI_SRC_RATE. CalDB maps are used.
46	LSS_RATE	Source count rate with coincidence-loss, aperture, and large-scale sensitivity corrections applied.
47	LSS_RATE_ERR	The 1σ error in LSS_RATE. This is computed by dividing AP_COI_SRC_RATE_ERR by LSS_FACTOR.
48	SENSCORR_FACTOR	Correction for the $\sim 1\%$ sensitivity loss per year to be applied to SENSCORR_RATE.
49	SENSCORR_RATE	Count rate with all corrections applied. LSS_RATE * SENSCORR_FACTOR.
50	SENSCORR_RATE_ERR	Errors on SENSCORR_RATE.
51	MAG	Magnitude of source in the UVOT system computed from SENSCORR_RATE. Value is set to 99.00 for upper-limits.
52	MAG_ERR	Error in MAG calculated using $\pm 2.5 log_{10}(1 + (\mathrm{SENSCORR\_RATE}/(\mathrm{COI\_BKG\_RATE} * \mathrm{SRC\_AREA}))^{-1})$. Value is set to 99.00 if MAG was an upper limit.
53	MAG_BKG	Sky magnitude, in magnitudes per square arcsecond, in the UVOT system corrected for SENSCORR_FACTOR and LSS_FACTOR. If COI_BKG_RATE is 0, it is set to 0.000004 for calculation purposes.
54	MAG_BKG_ERR	The 1σ error in MAG_BKG.
55	MAG_LIM	The "N"-sigma limiting magnitude in the UVOT system.
56	MAG_LIM_SIG	"N" for MAG_LIM, where "N" is a chosen parameter. The database uses a value of 2.0 for N.
57	MAG_COI_LIM	Magnitude at which the count rate is one count per CCD frame.
58	FLUX_AA	Flux density based on an average GRB spectrum, in $\mathrm{erg\,cm^{-2}\,s^{-1}\,\AA^{-1}}$.
59	FLUX_AA_ERR	The 1σ error in FLUX_AA.
60	FLUX_AA_BKG	Flux density of the sky in $\mathrm{erg\,cm^{-2}\,s^{-1}\,\AA^{-1}}$ per square arcsecond.
61	FLUX_AA_BKG_ERR	The 1σ error in FLUX_AA_BKG.
62	FLUX_AA_LIM	Approximate flux density limit in $\mathrm{erg\,cm^{-2}\,s^{-1}\,\AA^{-1}}$.
63	FLUX_AA_COI_LIM	Flux density at which the count rate is one count per frame time, in $\mathrm{erg\,cm^{-2}\,s^{-1}\,\AA^{-1}}$.
64	FLUX_HZ	Flux density in mJy.
65	FLUX_HZ_ERR	The 1σ error in FLUX_HZ.
66	FLUX_HZ_BKG	Flux density of the sky in mJy per square arcsecond.
67	FLUX_HZ_BKG_ERR	The 1σ error in FLUX_HZ_BKG.
68	FLUX_HZ_LIM	"N"-sigma limiting flux density in mJy, corresponding to MAG_LIM.
69	FLUX_HZ_COI_LIM	Flux density at which the count rate is one count per frame time, in mJy.
70	COI_RATE_LIMIT	Rate at which the coincidence loss becomes non-linear and can no longer be corrected.

Table 4 continued on next page

Table 4 *(continued)*

Column	Label	Description
71	NSIGMA	Significance of the detection.
72	FRAMTIME	Readout time for detector frame which includes deadtime correction.
73	SETTLE_FLAG	Settling images sometimes have a poor aspect solution which creates doublets out of field stars. Settling images also suffer from detector gain issues because the high voltages may still be ramping up part way into the exposure. Such images have an undefined photometric calibration and should be used cautiously. Images fitting all of the following are flagged as settling exposures, i.e. this flag is true (T): first exposure of Segment 0, image taken in Event mode, and EXPOSURE < 11 s.
74	ASPECT_FLAG	*Swift* spacecraft pointing accuracy is $\approx 5''$. The astrometric error is improved to about $0''.3$ by comparing source positions to the USNO-B catalog. For a small number of images the automated procedure did not produce an aspect solution. Such images are flagged as true (T).
75	TRAIL_FLAG	A number of images suffer from exposure of the CCD during readout clocking (cf. Page et al. 2013). Visible bright streaks along CCD columns (RAWY) sometimes complicate photometric measurements. These images are flagged true (T).
76	CROWDED_FLAG	If field appears crowded upon visual inspection image is flagged true (T).
77	SPIKE_FLAG	If a diffraction spike impinges upon the source region then the image is flagged true (T).
78	EDGE_FLAG	If source is sufficiently close to the edge of the image such that the exposure across the background region is variable then the image is flagged true (T).
79	HALO_FLAG	A few bursts lie within the halo of bright stars, which can produce inaccurate photometric measurements. Such situations are flagged by comparing the local background to the global background. These images are flagged true (T).
80	QUALITY_FLAG	Cumulative quality flag. This flag is set to true (T) when any of the following quality flags are true (T): SETTLE_FLAG, ASPECT_FLAG, TRAIL_FLAG, CROWDED_FLAG, SPIKE_FLAG, EDGE_FLAG, or HALO_FLAG.
81	IMAGE	Input name and FITS extension (e.g. sw00020004001ubb_sk.img.gz[3]). Names for images and event lists end with *.img.gz and *.evt.gz, respectively.

Table 5. NOC Database Description

Column	Label	Description
1	OBJECT	Same description as for column 1 of the image/event database.
2	FILTER	Same description as for column 13 of the image/event database.
3	TIME	Weighted time of the detection as described in M08.
4	TSTART	MET start time of the data used in the optimal co-addition.
5	TSTOP	MET stop time of the data used in the optimal co-addition.
6	EXPOSURE	Total exposure time in seconds for the optimally co-added data. Exposure time includes all corrections described in column 12 of the image/event database.
7	CSRC	Computed source counts in a co-added image as described in M08.
8	CERR	Uncertainty in the source counts of a co-added image as described in M08.
9	RATE	Computed co-added source rate calculated using (CSRC * SCALE_FACT) / EXPOSURE.
10	RATE_ERR	Source rate error calculated using (CERR * SCALE_FACT) / EXPOSURE.
11	MAG	Magnitude of the source in the UVOT system computed from RATE.
12	MAG_ERR	Same description as for column 52 of the image/event database.
13	FLUX	Same description as for column 58 of the image/event database.
14	FLUX_ERR	Same description as for column 59 of the image/event database.
15	SIGMA	Signal-to-noise of the co-added weighted image as described in M08.
16	FIT_START	Start time of the segment of the light curve used for normalization.
17	FIT_STOP	Stop time of the segment of the light curve used for normalization.
18	ALPHA	Temporal slope between FIT_START and FIT_STOP used for normalization.
19	SCALE_FACT	Normalization value used to scale the data taken in FILTER to NORM_TO.
20	NORM_TO	UVOT filter to which all filters have been normalized (uvw2, uvm2, uvw1, *u*, *b*, *v*, or *white*).

Table 6. Description of *Swift*/UVOT Burst Catalog

Column	Label	Description
1	OBJECT	Same description as for column 1 of the image/event database.
2	RA	Best available J2000 right ascension in decimal degrees.
3	DEC	Best available J2000 declination in decimal degrees.
4	POS_ERR	Positional uncertainty in arcseconds. If no positional uncertainty is available, value is set to -1.00.
5	POS_REF	Position reference for columns 2-4. References are from the SGA, GCN Circulars, Goad et al. (2007, 2008), or Butler (2007).
6	DISC_BY	The "discovery flag" indicating which spacecraft discovered the GRB. The flag is an integer from 0-7 representing: 0 = *Swift*, 1 = HETE2, 2 = INTEGRAL, 3 = IPN, 4 = *Fermi*, 5 = BAT Slew Survey (BATSS), 6 = AGILE, and 7 = *Swift* ground analysis.
7	TRIGTIME	Same description as for column 5 of the image/event database.
8	TRIG_UT	Same description as for column 6 of the image/event database.
9	Z	Redshift of the GRB from the SGA or Fynbo et al. (2009). If no redshift is available, value is set to -1.00.
10	E(B-V)_MW	Mean Milky Way E(B-V) from Schlafly & Finkbeiner (2011) found at IRSA[a].
11	E(B-V)_HOST	GRB host galaxy E(B-V) from Schady et al. (2010, 2012). If no value is available, value is set to -99.00.
12	T90	T_{90} in seconds.
13	T90_REF	T_{90} is from the SGA, or GCN Circulars when not available in the SGA.
14	BAT_FL	BAT fluence in the 15-150 keV range in $\mathrm{erg\,cm^{-2}}$. If not observed by BAT or data is not available in the SGA, value is set to -1.0000E-07.
15	BAT_FL_ERR	BAT fluence 90% error in the 15-150 keV range in $\mathrm{erg\,cm^{-2}}$. If not observed by BAT or data is not available in the SGA, value is set to -1.0000E-07.
16	BAT_PPF	BAT 1-second peak photon flux in the 15-150 keV range in $\mathrm{ph\,cm^{-2}\,s^{-1}}$. If not observed by BAT or data is not available in the SGA, value is set to -1.00.
17	BAT_PPF_ERR	BAT 1-second peak photon flux 90% error in the 15-150 keV range in $\mathrm{ph\,cm^{-2}\,s^{-1}}$. If not observed by BAT or data is not available in the SGA, value is set to -1.00.
18	BAT_PI	BAT photon index in the 15-150 keV range. If not observed by BAT or data is not available in the SGA, value is set to -1.00.
19	BAT_PIT	BAT photon index type. PL = a simple power-law; CPL = cutoff power-law. If not observed by BAT or data is not available in the SGA, value is set to NULL.
20	BAT_PI_ERR	BAT photon index 90% error in the 15-150 keV range. If not observed by BAT or data is not available in the SGA, value is set to -1.00.
21	XRT_FRST_OBS	Start time of the first XRT observation measured in seconds from the burst trigger. If not observed by XRT or data is not available in the SGA, value is set to -1.00.

Table 6 continued on next page

Table 6 *(continued)*

Column	Label	Description
22	XRT_FLUX	Early XRT flux in the 0.3-10 keV range in $\mathrm{erg\,cm^{-2}\,s^{-1}}$. If not observed by XRT or data is not available in the SGA, value is set to -1.0000E-11.
23	XRT_11FLUX	Same as for XRT_FLUX but at 11-hours.
24	XRT_24FLUX	Same as for XRT_FLUX but at 24-hours.
25	XRT_TI	Initial XRT temporal index. If not observed by XRT or data is not available in the SGA, value is set to 99.0000.
26	XRT_SI	XRT spectral index. If not observed by XRT or data is not available in the SGA, value is set to 99.0000.
27	XRT_NH	XRT column density in $\mathrm{cm^{-2}}$. If not observed by XRT or data is not available in the SGA, value is set to -1.00000E+21.
28	FRST_TSTART	Start time of first UVOT observation measured in seconds from the burst trigger. If not observed by UVOT, value is set to -1.0.
29	FRST_FILT	UVOT filter used for the FRST_TSTART exposure (uvw2, uvm2, uvw1, *u*, *b*, *v*, and *white*). If not observed by UVOT, value is set to NULL.
30	FRST_MAG	Magnitude of the FRST_TSTART observation. If no detections are reported, or not observed, value is set to 99.00.
31	FRST_MAG_ERR	The 1σ error on FRST_MAG. If no detections are reported for FRST_MAG, value is set to 99.00.
32	FRST_FLUX	Flux density of the FRST_TSTART observation in $\mathrm{erg\,cm^{-2}\,s^{-1}\,\AA^{-1}}$. If no detections are reported for FRST_MAG, value is set to 0.000000E+00.
33	FRST_FLUX_ERR	The 1σ error in FRST_FLUX. If no detections are reported for FRST_MAG, value is set to 0.000000E+00.
34	FRST_SIGMA	Significance of the FRST_MAG detection. If no detection is reported for FRST_MAG, value is set to 0.00.
35	PEAK_TSTART	Same description for column 28 immediately above, but for the peak values.
36	PEAK_FILT	Same description for column 29 immediately above, but for the peak values.
37	PEAK_MAG	Same description for column 30 immediately above, but for the peak values.
38	PEAK_MAG_ERR	Same description for column 31 immediately above, but for the peak values.
39	PEAK_FLUX	Same description for column 32 immediately above, but for the peak values.
40	PEAK_FLUX_ERR	Same description for column 33 immediately above, but for the peak values.
41	PEAK_SIGMA	Same description for column 34 immediately above, but for the peak values.
42	ALP1_W2	Temporal slope (α_{uvw2}) for the first segment of the light curve in the uvw2-filter. In the case of two or more afterglow detections in the pre-normalized uvw2 light curve, a temporal slope is calculated. Otherwise the value is set to -99.99. The value is calculated using $F(t) = At^{\alpha}$, where $F(t)$ is the flux density, A is the amplitude, and t is the time since burst.
43	ALP1N_W2	Negative 1σ error in ALP1_W2. If ALP1_W2 = -99.99 then ALP1N_W2 is set to -99.99.
44	ALP1P_W2	Positive 1σ error in ALP1_W2. If ALP1_W2 = -99.99 then ALP1P_W2 is set to -99.99.

Table 6 continued on next page

Table 6 *(continued)*

Column	Label	Description
45	TB1_W2	Break time between segment one and two of the uvw2 light curve. If there is no second segment, value is set -1.000000E+00.
46	TB1N_W2	TB1_W2 negative 1σ error. If TB1_W2 = -1.000000E+00 then TB1N_W2 is set to 0.000000E+00.
47	TB1P_W2	TB1_W2 positive 1σ error. If TB1_W2 = -1.000000E+00 then TB1P_W2 is set to 0.000000E+00.
48	ALP2_W2	In the event that a second segment of the light curve exists, a temporal slope is calculated for the segment. Otherwise the value is set to -99.99.
49	ALP2N_W2	Same description for column 43 immediately above, but for ALP2_W2.
50	ALP2P_W2	Same description for column 44 immediately above, but for ALP2_W2.
51	TB2_W2	Break time between segment two and three of the uvw2 light curve. If there is no third segment, value is set -1.000000E+00.
52	TB2N_W2	Same description for column 46 immediately above, but for TB2_W2.
53	TB2P_W2	Same description for column 47 immediately above, but for TB2_W2.
54	ALP3_W2	In the event that a third segment of the light curve exists, a temporal slope is calculated for the segment. Otherwise the value is set to -99.99.
55	ALP3N_W2	Same description for column 43 immediately above, but for ALP3_W2.
56	ALP3P_W2	Same description for column 44 immediately above, but for ALP3_W2.
57	TB3_W2	Break time between segment three and four of the uvw2 light curve. If there is no fourth segment, value is set -1.000000E+00.
58	TB3N_W2	Same description for column 46 immediately above, but for TB3_W2.
59	TB3P_W2	Same description for column 47 immediately above, but for TB3_W2.
60	ALP4_W2	In the event that a fourth segment of the light curve exists, a temporal slope is calculated for the segment. Otherwise the value is set to -99.99.
61	ALP4N_W2	Same description for column 43 immediately above, but for ALP4_W2.
62	ALP4P_W2	Same description for column 44 immediately above, but for ALP4_W2.
63	NORM_W2	Normalization factor (or A) for the first segment. This value is set -1.000000E+00 if ALP1_W2 is -99.99.
64	NORMN_W2	Negative 1σ error in NORM_W2. If NORM_W2 = -1.000000E+00 then NORMN_W2 is set to 0.000000E+00.
65	NORMP_W2	Positive 1σ error in NORM_W2. If NORM_W2 = -1.000000E+00 then NORMP_W2 is set to 0.000000E+00.
66	CHISQ_W2	The χ^2 value determined from the fit to the uvw2 light curve. If there is no fit, value is set to -1.00000.
67	DOF_W2	Degrees-of-freedom associated with CHISQ_W2. If there is no fit, value is set to -1.
68	ALP1_M2	Same description for column 42 immediately above, but for the uvm2-filter.
69	ALP1N_M2	Same description for column 43 immediately above, but for the uvm2-filter.
70	ALP1P_M2	Same description for column 44 immediately above, but for the uvm2-filter.

Table 6 continued on next page

Table 6 *(continued)*

Column	Label	Description
71	TB1_M2	Same description for column 45 immediately above, but for the uvm2-filter.
72	TB1N_M2	Same description for column 46 immediately above, but for the uvm2-filter.
73	TB1P_M2	Same description for column 47 immediately above, but for the uvm2-filter.
74	ALP2_M2	Same description for column 48 immediately above, but for the uvm2-filter.
75	ALP2N_M2	Same description for column 49 immediately above, but for the uvm2-filter.
76	ALP2P_M2	Same description for column 50 immediately above, but for the uvm2-filter.
77	TB2_M2	Same description for column 51 immediately above, but for the uvm2-filter.
78	TB2N_M2	Same description for column 52 immediately above, but for the uvm2-filter.
79	TB2P_M2	Same description for column 53 immediately above, but for the uvm2-filter.
80	ALP3_M2	Same description for column 54 immediately above, but for the uvm2-filter.
81	ALP3N_M2	Same description for column 55 immediately above, but for the uvm2-filter.
82	ALP3P_M2	Same description for column 56 immediately above, but for the uvm2-filter.
83	TB3_M2	Same description for column 57 immediately above, but for the uvm2-filter.
84	TB3N_M2	Same description for column 58 immediately above, but for the uvm2-filter.
85	TB3P_M2	Same description for column 59 immediately above, but for the uvm2-filter.
86	ALP4_M2	Same description for column 60 immediately above, but for the uvm2-filter.
87	ALP4N_M2	Same description for column 61 immediately above, but for the uvm2-filter.
88	ALP4P_M2	Same description for column 62 immediately above, but for the uvm2-filter.
89	NORM_M2	Same description for column 63 immediately above, but for the uvm2-filter.
90	NORMN_M2	Same description for column 64 immediately above, but for the uvm2-filter.
91	NORMP_M2	Same description for column 65 immediately above, but for the uvm2-filter.
92	CHISQ_M2	Same description for column 66 immediately above, but for the uvm2-filter.
93	DOF_M2	Same description for column 67 immediately above, but for the uvm2-filter.
94	ALP1_W1	Same description for column 42 immediately above, but for the uvw1-filter.
95	ALP1N_W1	Same description for column 43 immediately above, but for the uvw1-filter.
96	ALP1P_W1	Same description for column 44 immediately above, but for the uvw1-filter.
97	TB1_W1	Same description for column 45 immediately above, but for the uvw1-filter.
98	TB1N_W1	Same description for column 46 immediately above, but for the uvw1-filter.
99	TB1P_W1	Same description for column 47 immediately above, but for the uvw1-filter.
100	ALP2_W1	Same description for column 48 immediately above, but for the uvw1-filter.
101	ALP2N_W1	Same description for column 49 immediately above, but for the uvw1-filter.
102	ALP2P_W1	Same description for column 50 immediately above, but for the uvw1-filter.
103	TB2_W1	Same description for column 51 immediately above, but for the uvw1-filter.
104	TB2N_W1	Same description for column 52 immediately above, but for the uvw1-filter.
105	TB2P_W1	Same description for column 53 immediately above, but for the uvw1-filter.
106	ALP3_W1	Same description for column 54 immediately above, but for the uvw1-filter.
107	ALP3N_W1	Same description for column 55 immediately above, but for the uvw1-filter.
108	ALP3P_W1	Same description for column 56 immediately above, but for the uvw1-filter.

Table 6 continued on next page

Table 6 *(continued)*

Column	Label	Description
109	TB3_W1	Same description for column 57 immediately above, but for the uvw1-filter.
110	TB3N_W1	Same description for column 58 immediately above, but for the uvw1-filter.
111	TB3P_W1	Same description for column 59 immediately above, but for the uvw1-filter.
112	ALP4_W1	Same description for column 60 immediately above, but for the uvw1-filter.
113	ALP4N_W1	Same description for column 61 immediately above, but for the uvw1-filter.
114	ALP4P_W1	Same description for column 62 immediately above, but for the uvw1-filter.
115	NORM_W1	Same description for column 63 immediately above, but for the uvw1-filter.
116	NORMN_W1	Same description for column 64 immediately above, but for the uvw1-filter.
117	NORMP_W1	Same description for column 65 immediately above, but for the uvw1-filter.
118	CHISQ_W1	Same description for column 66 immediately above, but for the uvw1-filter.
119	DOF_W1	Same description for column 67 immediately above, but for the uvw1-filter.
120	ALP1_UU	Same description for column 42 immediately above, but for the u-filter.
121	ALP1N_UU	Same description for column 43 immediately above, but for the u-filter.
122	ALP1P_UU	Same description for column 44 immediately above, but for the u-filter.
123	TB1_UU	Same description for column 45 immediately above, but for the u-filter.
124	TB1N_UU	Same description for column 46 immediately above, but for the u-filter.
125	TB1P_UU	Same description for column 47 immediately above, but for the u-filter.
126	ALP2_UU	Same description for column 48 immediately above, but for the u-filter.
127	ALP2N_UU	Same description for column 49 immediately above, but for the u-filter.
128	ALP2P_UU	Same description for column 50 immediately above, but for the u-filter.
129	TB2_UU	Same description for column 51 immediately above, but for the u-filter.
130	TB2N_UU	Same description for column 52 immediately above, but for the u-filter.
131	TB2P_UU	Same description for column 53 immediately above, but for the u-filter.
132	ALP3_UU	Same description for column 54 immediately above, but for the u-filter.
133	ALP3N_UU	Same description for column 55 immediately above, but for the u-filter.
134	ALP3P_UU	Same description for column 56 immediately above, but for the u-filter.
135	TB3_UU	Same description for column 57 immediately above, but for the u-filter.
136	TB3N_UU	Same description for column 58 immediately above, but for the u-filter.
137	TB3P_UU	Same description for column 59 immediately above, but for the u-filter.
138	ALP4_UU	Same description for column 60 immediately above, but for the u-filter.
139	ALP4N_UU	Same description for column 61 immediately above, but for the u-filter.
140	ALP4P_UU	Same description for column 62 immediately above, but for the u-filter.
141	NORM_UU	Same description for column 63 immediately above, but for the u-filter.
142	NORMN_UU	Same description for column 64 immediately above, but for the u-filter.
143	NORMP_UU	Same description for column 65 immediately above, but for the u-filter.
144	CHISQ_UU	Same description for column 66 immediately above, but for the u-filter.
145	DOF_UU	Same description for column 67 immediately above, but for the u-filter.
146	ALP1_BB	Same description for column 42 immediately above, but for the b-filter.

Table 6 continued on next page

Table 6 *(continued)*

Column	Label	Description
147	ALP1N_BB	Same description for column 43 immediately above, but for the *b*-filter.
148	ALP1P_BB	Same description for column 44 immediately above, but for the *b*-filter.
149	TB1_BB	Same description for column 45 immediately above, but for the *b*-filter.
150	TB1N_BB	Same description for column 46 immediately above, but for the *b*-filter.
151	TB1P_BB	Same description for column 47 immediately above, but for the *b*-filter.
152	ALP2_BB	Same description for column 48 immediately above, but for the *b*-filter.
153	ALP2N_BB	Same description for column 49 immediately above, but for the *b*-filter.
154	ALP2P_BB	Same description for column 50 immediately above, but for the *b*-filter.
155	TB2_BB	Same description for column 51 immediately above, but for the *b*-filter.
156	TB2N_BB	Same description for column 52 immediately above, but for the *b*-filter.
157	TB2P_BB	Same description for column 53 immediately above, but for the *b*-filter.
158	ALP3_BB	Same description for column 54 immediately above, but for the *b*-filter.
159	ALP3N_BB	Same description for column 55 immediately above, but for the *b*-filter.
160	ALP3P_BB	Same description for column 56 immediately above, but for the *b*-filter.
161	TB3_BB	Same description for column 57 immediately above, but for the *b*-filter.
162	TB3N_BB	Same description for column 58 immediately above, but for the *b*-filter.
163	TB3P_BB	Same description for column 59 immediately above, but for the *b*-filter.
164	ALP4_BB	Same description for column 60 immediately above, but for the *b*-filter.
165	ALP4N_BB	Same description for column 61 immediately above, but for the *b*-filter.
166	ALP4P_BB	Same description for column 62 immediately above, but for the *b*-filter.
167	NORM_BB	Same description for column 63 immediately above, but for the *b*-filter.
168	NORMN_BB	Same description for column 64 immediately above, but for the *b*-filter.
169	NORMP_BB	Same description for column 65 immediately above, but for the *b*-filter.
170	CHISQ_BB	Same description for column 66 immediately above, but for the *b*-filter.
171	DOF_BB	Same description for column 67 immediately above, but for the *b*-filter.
172	ALP1_VV	Same description for column 42 immediately above, but for the *v*-filter.
173	ALP1N_VV	Same description for column 43 immediately above, but for the *v*-filter.
174	ALP1P_VV	Same description for column 44 immediately above, but for the *v*-filter.
175	TB1_VV	Same description for column 45 immediately above, but for the *v*-filter.
176	TB1N_VV	Same description for column 46 immediately above, but for the *v*-filter.
177	TB1P_VV	Same description for column 47 immediately above, but for the *v*-filter.
178	ALP2_VV	Same description for column 48 immediately above, but for the *v*-filter.
179	ALP2N_VV	Same description for column 49 immediately above, but for the *v*-filter.
180	ALP2P_VV	Same description for column 50 immediately above, but for the *v*-filter.
181	TB2_VV	Same description for column 51 immediately above, but for the *v*-filter.
182	TB2N_VV	Same description for column 52 immediately above, but for the *v*-filter.
183	TB2P_VV	Same description for column 53 immediately above, but for the *v*-filter.
184	ALP3_VV	Same description for column 54 immediately above, but for the *v*-filter.

Table 6 continued on next page

Table 6 *(continued)*

Column	Label	Description
185	ALP3N_VV	Same description for column 55 immediately above, but for the *v*-filter.
186	ALP3P_VV	Same description for column 56 immediately above, but for the *v*-filter.
187	TB3_VV	Same description for column 57 immediately above, but for the *v*-filter.
188	TB3N_VV	Same description for column 58 immediately above, but for the *v*-filter.
189	TB3P_VV	Same description for column 59 immediately above, but for the *v*-filter.
190	ALP4_VV	Same description for column 60 immediately above, but for the *v*-filter.
191	ALP4N_VV	Same description for column 61 immediately above, but for the *v*-filter.
192	ALP4P_VV	Same description for column 62 immediately above, but for the *v*-filter.
193	NORM_VV	Same description for column 63 immediately above, but for the *v*-filter.
194	NORMN_VV	Same description for column 64 immediately above, but for the *v*-filter.
195	NORMP_VV	Same description for column 65 immediately above, but for the *v*-filter.
196	CHISQ_VV	Same description for column 66 immediately above, but for the *v*-filter.
197	DOF_VV	Same description for column 67 immediately above, but for the *v*-filter.
198	ALP1_WH	Same description for column 42 immediately above, but for the *white*-filter.
199	ALP1N_WH	Same description for column 43 immediately above, but for the *white*-filter.
200	ALP1P_WH	Same description for column 44 immediately above, but for the *white*-filter.
201	TB1_WH	Same description for column 45 immediately above, but for the *white*-filter.
202	TB1N_WH	Same description for column 46 immediately above, but for the *white*-filter.
203	TB1P_WH	Same description for column 47 immediately above, but for the *white*-filter.
204	ALP2_WH	Same description for column 48 immediately above, but for the *white*-filter.
205	ALP2N_WH	Same description for column 49 immediately above, but for the *white*-filter.
206	ALP2P_WH	Same description for column 50 immediately above, but for the *white*-filter.
207	TB2_WH	Same description for column 51 immediately above, but for the *white*-filter.
208	TB2N_WH	Same description for column 52 immediately above, but for the *white*-filter.
209	TB2P_WH	Same description for column 53 immediately above, but for the *white*-filter.
210	ALP3_WH	Same description for column 54 immediately above, but for the *white*-filter.
211	ALP3N_WH	Same description for column 55 immediately above, but for the *white*-filter.
212	ALP3P_WH	Same description for column 56 immediately above, but for the *white*-filter.
213	TB3_WH	Same description for column 57 immediately above, but for the *white*-filter.
214	TB3N_WH	Same description for column 58 immediately above, but for the *white*-filter.
215	TB3P_WH	Same description for column 59 immediately above, but for the *white*-filter.
216	ALP4_WH	Same description for column 60 immediately above, but for the *white*-filter.
217	ALP4N_WH	Same description for column 61 immediately above, but for the *white*-filter.
218	ALP4P_WH	Same description for column 62 immediately above, but for the *white*-filter.
219	NORM_WH	Same description for column 63 immediately above, but for the *white*-filter.
220	NORMN_WH	Same description for column 64 immediately above, but for the *white*-filter.
221	NORMP_WH	Same description for column 65 immediately above, but for the *white*-filter.
222	CHISQ_WH	Same description for column 66 immediately above, but for the *white*-filter.

Table 6 continued on next page

Table 6 *(continued)*

Column	Label	Description
223	DOF_WH	Same description for column 67 immediately above, but for the *white*-filter.
224	R2_2E3_W2	Count rate calculated at 2×10^3 s from the respective uvw2 temporal slope. Value is set to -1.00000E+00 if no temporal slope is available.
225	R2_ERN_2E3_W2	R2_2E3_W2 negative error. If R2_2E3_W2 = -1.00000E+00, value set to -1.00000E+00.
226	R2_ERP_2E3_W2	R2_2E3_W2 positive error. If R2_2E3_W2 = -1.00000E+00, value set to -1.00000E+00.
227	F2_2E3_W2	R2_2E3_W2 converted into flux density in $\mathrm{erg\,s^{-1}\,cm^{-2}\,\AA^{-1}}$. This value is corrected for Milky Way extinction using the methods described by Cardelli et al. (1989) and Gordon et al. (2009, 2014), and is further corrected for redshifted host extinction using the method described in Pei (1992)[b]. We assume a SMC dust for the host based on results from Schady et al. (2010). If E(B-V)_HOST = -99.0000, the value is set to 0.1, which is the average host extinction found by Schady et al. (2012). If no redshift is available, the value is set to 1.2517, the mean value of our UVOT detected sample. If R2_2E3_W2 = -1.00000E+00, then F2_2E3_W2 = -1.000E+00. For calculation purposes, if this value is 0.000E+00, it is set to 1.000E-23.
228	F2_ERN_2E3_W2	F2_2E3_W2 negative error. If F2_2E3_W2 = -1.00000E+00, value set to -1.00000E+00. For calculation purposes, if F2_2E3_W2 = 0.000E+00, it is set to 1.000E-23.
229	F2_ERP_2E3_W2	F2_2E3_W2 positive error. If F2_2E3_W2 = -1.00000E+00, value set to -1.00000E+00. For calculation purposes, if F2_2E3_W2 = 0.000E+00, it is set to 1.000E-23.
230	R2_2E3_M2	Same description for column 224 immediately above, but for the uvm2-filter.
231	R2_ERN_2E3_M2	Same description for column 225 immediately above, but for the uvm2-filter.
232	R2_ERP_2E3_M2	Same description for column 226 immediately above, but for the uvm2-filter.
233	F2_2E3_M2	Same description for column 227 immediately above, but for the uvm2-filter.
234	F2_ERN_2E3_M2	Same description for column 228 immediately above, but for the uvm2-filter.
235	F2_ERP_2E3_M2	Same description for column 229 immediately above, but for the uvm2-filter.
236	R2_2E3_W1	Same description for column 224 immediately above, but for the uvw1-filter.
237	R2_ERN_2E3_W1	Same description for column 225 immediately above, but for the uvw1-filter.
238	R2_ERP_2E3_W1	Same description for column 226 immediately above, but for the uvw1-filter.
239	F2_2E3_W1	Same description for column 227 immediately above, but for the uvw1-filter.
240	F2_ERN_2E3_W1	Same description for column 228 immediately above, but for the uvw1-filter.
241	F2_ERP_2E3_W1	Same description for column 229 immediately above, but for the uvw1-filter.
242	R2_2E3_UU	Same description for column 224 immediately above, but for the *u*-filter.
243	R2_ERN_2E3_UU	Same description for column 225 immediately above, but for the *u*-filter.
244	R2_ERP_2E3_UU	Same description for column 226 immediately above, but for the *u*-filter.
245	F2_2E3_UU	Same description for column 227 immediately above, but for the *u*-filter.
246	F2_ERN_2E3_UU	Same description for column 228 immediately above, but for the *u*-filter.
247	F2_ERP_2E3_UU	Same description for column 229 immediately above, but for the *u*-filter.
248	R2_2E3_BB	Same description for column 224 immediately above, but for the *b*-filter.
249	R2_ERN_2E3_BB	Same description for column 225 immediately above, but for the *b*-filter.

Table 6 continued on next page

Table 6 *(continued)*

Column	Label	Description
250	R2_ERP_2E3_BB	Same description for column 226 immediately above, but for the b-filter.
251	F2_2E3_BB	Same description for column 227 immediately above, but for the b-filter.
252	F2_ERN_2E3_BB	Same description for column 228 immediately above, but for the b-filter.
253	F2_ERP_2E3_BB	Same description for column 229 immediately above, but for the b-filter.
254	R2_2E3_VV	Same description for column 224 immediately above, but for the v-filter.
255	R2_ERN_2E3_VV	Same description for column 225 immediately above, but for the v-filter.
256	R2_ERP_2E3_VV	Same description for column 226 immediately above, but for the v-filter.
257	F2_2E3_VV	Same description for column 227 immediately above, but for the v-filter.
258	F2_ERN_2E3_VV	Same description for column 228 immediately above, but for the v-filter.
259	F2_ERP_2E3_VV	Same description for column 229 immediately above, but for the v-filter.
260	R2_2E4_W2	Same description for column 224 immediately above, but calculated at 2×10^4 s.
261	R2_ERN_2E4_W2	Same description for column 225 immediately above, but calculated at 2×10^4 s.
262	R2_ERP_2E4_W2	Same description for column 226 immediately above, but calculated at 2×10^4 s.
263	F2_2E4_W2	Same description for column 227 immediately above, but calculated at 2×10^4 s.
264	F2_ERN_2E4_W2	Same description for column 228 immediately above, but calculated at 2×10^4 s.
265	F2_ERP_2E4_W2	Same description for column 229 immediately above, but calculated at 2×10^4 s.
266	R2_2E4_M2	Same description for column 230 immediately above, but calculated at 2×10^4 s.
267	R2_ERN_2E4_M2	Same description for column 231 immediately above, but calculated at 2×10^4 s.
268	R2_ERP_2E4_M2	Same description for column 232 immediately above, but calculated at 2×10^4 s.
269	F2_2E4_M2	Same description for column 233 immediately above, but calculated at 2×10^4 s.
270	F2_ERN_2E4_M2	Same description for column 234 immediately above, but calculated at 2×10^4 s.
271	F2_ERP_2E4_M2	Same description for column 235 immediately above, but calculated at 2×10^4 s.
272	R2_2E4_W1	Same description for column 236 immediately above, but calculated at 2×10^4 s.
273	R2_ERN_2E4_W1	Same description for column 237 immediately above, but calculated at 2×10^4 s.
274	R2_ERP_2E4_W1	Same description for column 238 immediately above, but calculated at 2×10^4 s.
275	F2_2E4_W1	Same description for column 239 immediately above, but calculated at 2×10^4 s.
276	F2_ERN_2E4_W1	Same description for column 240 immediately above, but calculated at 2×10^4 s.
277	F2_ERP_2E4_W1	Same description for column 241 immediately above, but calculated at 2×10^4 s.
278	R2_2E4_UU	Same description for column 242 immediately above, but calculated at 2×10^4 s.
279	R2_ERN_2E4_UU	Same description for column 243 immediately above, but calculated at 2×10^4 s.
280	R2_ERP_2E4_UU	Same description for column 244 immediately above, but calculated at 2×10^4 s.
281	F2_2E4_UU	Same description for column 245 immediately above, but calculated at 2×10^4 s.
282	F2_ERN_2E4_UU	Same description for column 246 immediately above, but calculated at 2×10^4 s.
283	F2_ERP_2E4_UU	Same description for column 247 immediately above, but calculated at 2×10^4 s.
284	R2_2E4_BB	Same description for column 248 immediately above, but calculated at 2×10^4 s.
285	R2_ERN_2E4_BB	Same description for column 249 immediately above, but calculated at 2×10^4 s.
286	R2_ERP_2E4_BB	Same description for column 250 immediately above, but calculated at 2×10^4 s.
287	F2_2E4_BB	Same description for column 251 immediately above, but calculated at 2×10^4 s.

Table 6 continued on next page

Table 6 *(continued)*

Column	Label	Description
288	F2_ERN_2E4_BB	Same description for column 252 immediately above, but calculated at 2×10^4 s.
289	F2_ERP_2E4_BB	Same description for column 253 immediately above, but calculated at 2×10^4 s.
290	R2_2E4_VV	Same description for column 254 immediately above, but calculated at 2×10^4 s.
291	R2_ERN_2E4_VV	Same description for column 255 immediately above, but calculated at 2×10^4 s.
292	R2_ERP_2E4_VV	Same description for column 256 immediately above, but calculated at 2×10^4 s.
293	F2_2E4_VV	Same description for column 257 immediately above, but calculated at 2×10^4 s.
294	F2_ERN_2E4_VV	Same description for column 258 immediately above, but calculated at 2×10^4 s.
295	F2_ERP_2E4_VV	Same description for column 259 immediately above, but calculated at 2×10^4 s.
296	R2_2E5_W2	Same description for column 224 immediately above, but calculated at 2×10^5 s.
297	R2_ERN_2E5_W2	Same description for column 225 immediately above, but calculated at 2×10^5 s.
298	R2_ERP_2E5_W2	Same description for column 226 immediately above, but calculated at 2×10^5 s.
299	F2_2E5_W2	Same description for column 227 immediately above, but calculated at 2×10^5 s.
300	F2_ERN_2E5_W2	Same description for column 228 immediately above, but calculated at 2×10^5 s.
301	F2_ERP_2E5_W2	Same description for column 229 immediately above, but calculated at 2×10^5 s.
302	R2_2E5_M2	Same description for column 230 immediately above, but calculated at 2×10^5 s.
303	R2_ERN_2E5_M2	Same description for column 231 immediately above, but calculated at 2×10^5 s.
304	R2_ERP_2E5_M2	Same description for column 232 immediately above, but calculated at 2×10^5 s.
305	F2_2E5_M2	Same description for column 233 immediately above, but calculated at 2×10^5 s.
306	F2_ERN_2E5_M2	Same description for column 234 immediately above, but calculated at 2×10^5 s.
307	F2_ERP_2E5_M2	Same description for column 235 immediately above, but calculated at 2×10^5 s.
308	R2_2E5_W1	Same description for column 236 immediately above, but calculated at 2×10^5 s.
309	R2_ERN_2E5_W1	Same description for column 237 immediately above, but calculated at 2×10^5 s.
310	R2_ERP_2E5_W1	Same description for column 238 immediately above, but calculated at 2×10^5 s.
311	F2_2E5_W1	Same description for column 239 immediately above, but calculated at 2×10^5 s.
312	F2_ERN_2E5_W1	Same description for column 240 immediately above, but calculated at 2×10^5 s.
313	F2_ERP_2E5_W1	Same description for column 241 immediately above, but calculated at 2×10^5 s.
314	R2_2E5_UU	Same description for column 242 immediately above, but calculated at 2×10^5 s.
315	R2_ERN_2E5_UU	Same description for column 243 immediately above, but calculated at 2×10^5 s.
316	R2_ERP_2E5_UU	Same description for column 244 immediately above, but calculated at 2×10^5 s.
317	F2_2E5_UU	Same description for column 245 immediately above, but calculated at 2×10^5 s.
318	F2_ERN_2E5_UU	Same description for column 246 immediately above, but calculated at 2×10^5 s.
319	F2_ERP_2E5_UU	Same description for column 247 immediately above, but calculated at 2×10^5 s.
320	R2_2E5_BB	Same description for column 248 immediately above, but calculated at 2×10^5 s.
321	R2_ERN_2E5_BB	Same description for column 249 immediately above, but calculated at 2×10^5 s.
322	R2_ERP_2E5_BB	Same description for column 250 immediately above, but calculated at 2×10^5 s.
323	F2_2E5_BB	Same description for column 251 immediately above, but calculated at 2×10^5 s.
324	F2_ERN_2E5_BB	Same description for column 252 immediately above, but calculated at 2×10^5 s.
325	F2_ERP_2E5_BB	Same description for column 253 immediately above, but calculated at 2×10^5 s.

Table 6 continued on next page

Table 6 *(continued)*

Column	Label	Description
326	R2_2E5_VV	Same description for column 254 immediately above, but calculated at 2×10^5 s.
327	R2_ERN_2E5_VV	Same description for column 255 immediately above, but calculated at 2×10^5 s.
328	R2_ERP_2E5_VV	Same description for column 256 immediately above, but calculated at 2×10^5 s.
329	F2_2E5_VV	Same description for column 257 immediately above, but calculated at 2×10^5 s.
330	F2_ERN_2E5_VV	Same description for column 258 immediately above, but calculated at 2×10^5 s.
331	F2_ERP_2E5_VV	Same description for column 259 immediately above, but calculated at 2×10^5 s.
332	BETA_2E3	Spectral slope at 2×10^3 s (β_{2E3}) as determined from F2_2E3_W2, F2_2E3_M2, F2_2E3_W1, F2_2E3_UU, F2_2E3_BB, and F2_2E3_VV after conversion to mJy. In the case of a detection in two or more filters, a spectral slope is calculated. The value is calculated using $F(\nu) = B\nu^{\beta}$, where $F(\nu)$ is the flux density in mJy, B is the normalization factor, and ν is the filter redshifted central frequency. To calculate β, we fit a straight line in log-log space to the data using LINEFIT in IDL. We then calculate the χ^2 fit of this line to the data points. The data have unequal plus and minus errors, therefore we conservatively use the greater of these errors in our calculation. If there are less than two data points this value is set to -99.00.
333	BETA_2E3_ERR	The 1σ error on BETA_2E3. If BETA_2E3 = -99.00, this value is set to -1.00.
334	NORM_2E3	Normalization factor (B) for spectral slope calculation. Value set to-1.0000E+00 if BETA_2E3 is -99.00. The maximum value is capped at 9.9900E+300.
335	NORM_2E3_ERR	Error on NORM_2E3. If NORM_2E3 = -1.0000E+00, this value is set to -1.0000E+00.
336	CHISQ_B3	The χ^2 value determined from the fit to the spectral slope at an epoch of 2×10^3 s. If there is no fit, value is set to -1.00000E+00.
337	DOF_B3	Degrees-of-freedom associated with CHISQ_B3. If there is no fit, value is set to -1.
338	BETA_2E4	Same description for column 332 immediately above, but calculated at 2×10^4 s.
339	BETA_2E4_ERR	Same description for column 333 immediately above, but calculated at 2×10^4 s.
340	NORM_2E4	Same description for column 334 immediately above, but calculated at 2×10^4 s.
341	NORM_2E4_ERR	Same description for column 335 immediately above, but calculated at 2×10^4 s.
342	CHISQ_B4	Same description for column 336 immediately above, but calculated at 2×10^4 s.
343	DOF_B4	Same description for column 337 immediately above, but calculated at 2×10^4 s.
344	BETA_2E5	Same description for column 332 immediately above, but calculated at 2×10^5 s.
345	BETA_2E5_ERR	Same description for column 333 immediately above, but calculated at 2×10^5 s.
346	NORM_2E5	Same description for column 334 immediately above, but calculated at 2×10^5 s.
347	NORM_2E5_ERR	Same description for column 335 immediately above, but calculated at 2×10^5 s.
348	CHISQ_B5	Same description for column 336 immediately above, but calculated at 2×10^5 s.
349	DOF_B5	Same description for column 337 immediately above, but calculated at 2×10^5 s.

[a] This research has made use of the NASA/IPAC Infrared Science Archive, which is operated by the Jet Propulsion Laboratory, California Institute of Technology, under contract with the National Aeronautics and Space Administration.

[b] We caution, that for convenience, we have extrapolated into the UV the Pei (1992) SMC empirical extinction curve beyond that published.

Table 7. *Swift*/UVOT GRB Catalog Parameter Means

Parameter	Mean	σ
z	2.04	1.39
E(B-V)$_{\rm Gal}$	0.20	1.43
E(B-V)$_{\rm Host}$	0.09	0.08
T_{90}	75.4 s	135.0 s
$T_{90} > 2$ s	82.7 s	139.4 s
$T_{90} \leq 2$ s	0.6 s	0.6 s
S_γ	3.17×10^{-6} erg cm^{-2}	7.38×10^{-6} erg cm^{-2}
$F_{X,e}$	1.03×10^{-8} erg cm^{-2} s^{-1}	3.90×10^{-8} erg cm^{-2} s^{-1}
N_H	4.86×10^{21} cm^{-2}	6.69×10^{21} cm^{-2}

NOTE—The mean is calculated only for those GRBs with measured parameters, therefore, each parameter mean will be represented by a different number of GRBs. The parameters are redshift (z), Milky Way reddening (E(B-V)$_{\rm Gal}$), host reddening (E(B-V)$_{\rm Host}$), all T_{90}, T_{90} for long bursts ($T_{90} > 2$ s), T_{90} for short bursts ($T_{90} \leq 2$ s), BAT fluence (S_γ), early XRT flux ($F_{X,e}$), and gas column density (N_H).

5. CATALOG SUMMARY

We present some of the general features from the UVOT GRB databases and catalog. Of the 538 UVOT observed GRBs, 62% (43%) are detected by the UVOT at the 2σ (3σ) level in optimally coadded exposures. This is comparable to the $\sim$ 50% detection rate by ground-based observations (cf. Fynbo et al. 2009) and an increase of $\sim$ 2 (for the 3σ value) from Paper1. The increased detection rate, as compared to Paper1, is attributed to the use of optimal coaddition. If the sample is subdivided into long ($T_{90} > 2$ s) and short ($T_{90} \leq 2$ s) bursts (Kouveliotou et al. 1993), then the detection rate for optimally coadded exposures is 63% (43%) and 49% (40%) for long and short bursts, respectively. The mean redshift (z), galactic reddening (E(B-V)$_{\rm Gal}$), host reddening (E(B-V)$_{\rm Host}$), T_{90}, $T_{90} > 2$ s, $T_{90} \leq 2$ s, BAT fluence (S_γ), early XRT flux ($F_{X,e}$), and the gas column density (N_H) for our sample are found in Table 7.

The mean magnitude of the first detections is 17.06 ($1\sigma = \pm 1.94$), with 11.43 and 21.71 mag for the brightest and faintest first magnitude, respectively (Figure 2-*Top Left*). The mean peak magnitude is 17.70 ($1\sigma = \pm 1.80$), with 11.41 and 22.43 mag for the brightest and faintest peak magnitude, respectively (Figure 2-*Top Right*). For bursts that meet the criteria time-to-observation < 500 s and Galactic reddening < 0.5 (cf. Fynbo et al. 2009), an afterglow is detected in an *optimally coadded* exposure 60% (41%) of the time. For time-to-observation of bursts ≥ 500 s and for Galactic reddening < 0.5, an afterglow is detected in an *optimally coadded* exposure 64% (44%) of the time. The remaining "dark" bursts are most likely explained by one or more of the following scenarios: the afterglow is below the detection threshold due to rapid temporal decay (cf. Roming et al. 2006b), high background due to small sun-to-field angle (cf. Fynbo et al. 2009), large Galactic extinction (cf. Fynbo et al. 2009), high circumburst extinction (cf. Roming et al. 2006b; D'Elia & Stratta 2012; Jeong et al. 2014), and Lyα damping due to high-redshift (cf. Roming et al. 2006b; D'Elia & Stratta 2012).

The median time to burst observation is 110.8 s (Figure 2-*Bottom Left*). The fastest time for an observation to begin is 37.8 s for GRB 050509B. The median time to a peak observation is 1600.2 s (Figure 2-*Bottom Right*). The fastest time to a peak observation is 39.8 s for GRB 050509A.

The distribution of the temporal slopes in the first segment for each filter are found in Figure 3. The mean temporal slopes ($\overline{\alpha}$) for each UVOT filter and lightcurve segment are provided in Table 8. The mean break times ($\overline{t_b}$) for the different segments in each filter, as well as the minimum (t_{b-min}) and maximum (t_{b-max}) break times per filter, are found in Table 9. An examination of the temporal slopes reveals a general shallow decline in the first segment followed

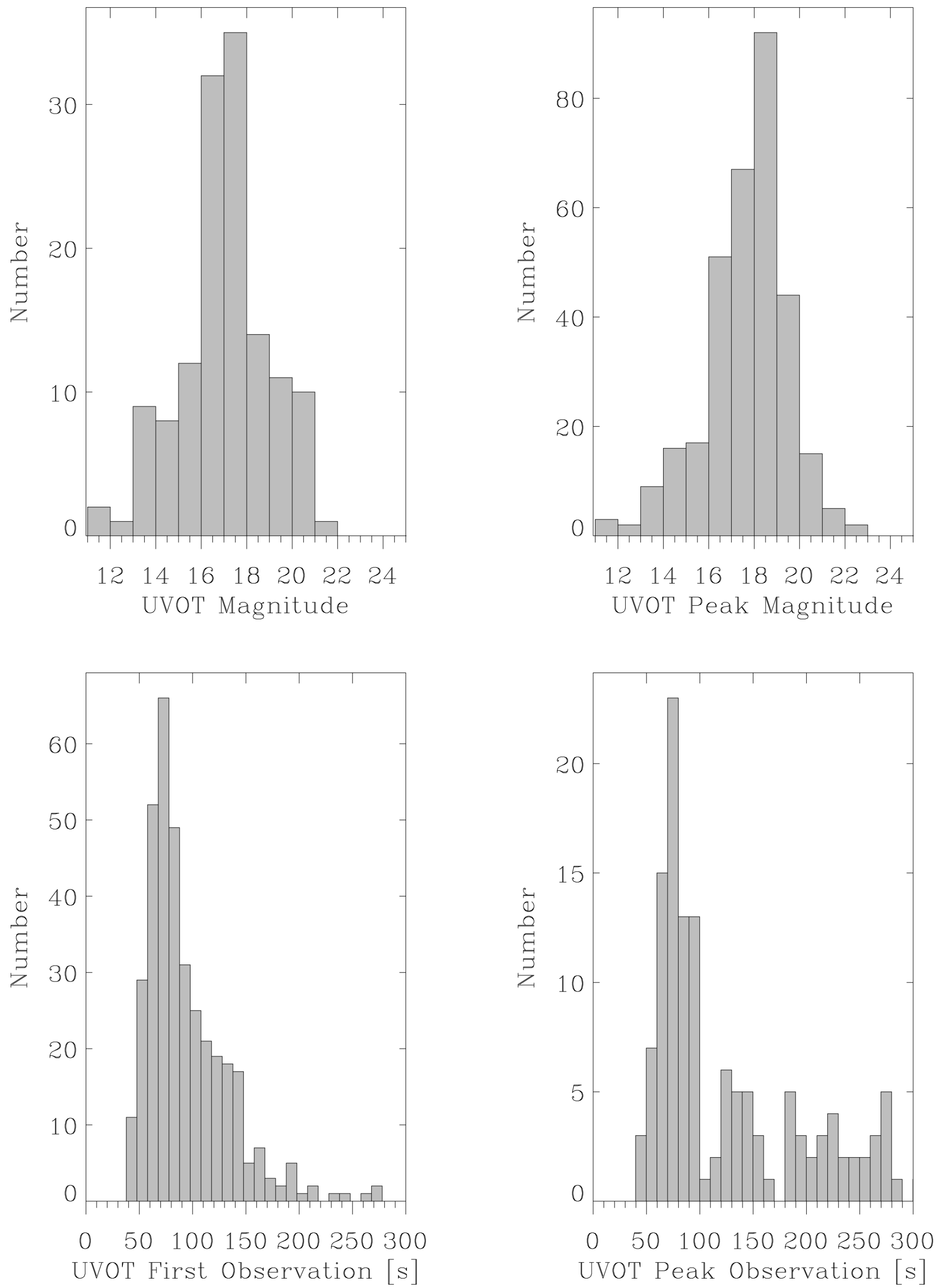

Figure 2. *Top Left:* Histogram of the magnitude of the first detections. *Top Right:* Histogram of the magnitude of the peak detections. *Bottom Left:* Histogram of the time since burst for first observation. Only the first 300 s are shown. *Bottom Right:* Histogram of the time to peak observations. Also, only the first 300 s are shown.

Table 8. Mean temporal slopes per segment per UVOT filter

UVOT Filter	$\overline{\alpha_1}$ (σ)	$\overline{\alpha_2}$ (σ)	$\overline{\alpha_3}$ (σ)	$\overline{\alpha_4}$ (σ)
uvw2	-0.24 (0.83)	-0.98 (1.06)	-2.19 (0.35)	-0.27 (—)
uvm2	-0.34 (0.73)	-0.87 (1.02)	-1.55 (1.27)	-0.28 (—)
uvw1	-0.55 (2.22)	-0.85 (1.42)	-0.52 (0.65)	— (—)
u	-0.56 (1.03)	-0.71 (1.02)	-0.47 (0.81)	-1.77 (0.22)
b	-0.56 (1.28)	-1.06 (1.85)	0.22 (1.23)	-1.56 (—)
v	-0.41 (0.82)	-0.66 (1.15)	-0.71 (0.65)	-1.23 (—)
white	-0.35 (1.50)	-0.47 (1.37)	-0.74 (0.74)	— (—)
all	-0.45 (1.30)	-0.70 (1.31)	-0.68 (0.90)	-1.15 (0.71)

Note—If no temporal slopes exist for a given filter (or σ cannot be calculated), the value is represented by —.

Table 9. Mean, minimum, and maximum break times ($\times 10^4$ s) per UVOT filter

UVOT Filter	$\overline{t_{b1}}$ (σ)	$\overline{t_{b2}}$ (σ)	$\overline{t_{b3}}$ (σ)	t_{b-min}	t_{b-max}
uvw2	5.14 (5.87)	9.85 (4.21)	32.43 (—)	0.04	32.43
uvm2	5.70 (6.19)	13.07 (13.41)	31.77 (—)	0.81	31.77
uvw1	11.94 (22.16)	52.92 (73.83)	— (—)	0.15	162.13
u	7.60 (23.03)	27.17 (45.04)	47.67 (47.93)	0.02	81.56
b	2.15 (3.00)	15.09 (11.94)	83.57 (—)	0.08	83.57
v	2.89 (6.20)	5.47 (7.75)	93.37 (—)	0.02	93.37
white	2.87 (9.41)	14.58 (27.18)	— (—)	0.01	83.56
all	4.69 (13.21)	17.43 (32.46)	56.08 (33.87)	0.01	162.13

Note—If no break time exist for a given filter (or σ cannot be calculated), the value is represented by —.

by a steepening in the second segment by a factor of ~ 2. For the bluest UV filters (uvw2 and uvm2), as well as the *white* filter, the transition from the second segment to the third is again steepened. In contrast, the remaining filters manifest the opposite behavior. Since there are fewer measured temporal slopes in the third and fourth segments, we caution that inferring any general trends using the individual filters in the later segments may provide erroneous conclusions.

If we take all the filters together, the trend starts shallow in the first segment, is more steep in the second, then a shallower slope in the third (although not as shallow as the first segment), and finally a steep decay. This general description does not behave the same as the "canonical" X-ray lightcurve (cf. Zhang et al. 2006; Nousek et al. 2006). However, from an examination of the individual normalized UVOT light curves, $\sim 7\%$, $\sim 7\%$, $\sim 14\%$, and $\sim 47\%$ are consistent with the "a," "b," "c," and "d" X-ray morphologies described in Evans et al. (2009) and illustrated in Figure 4. Of the remaining $\sim 25\%$, $\sim 21\%$ have the new morphology "e" and $\sim 4\%$ have the "f" morphology as illustrated in Figure 4. Morphology "e" echoes a somewhat similar profile to that described above when all filters are taken together. The profile starts with a gentle rise in the first segment, transitioning to a steep decay in the second,

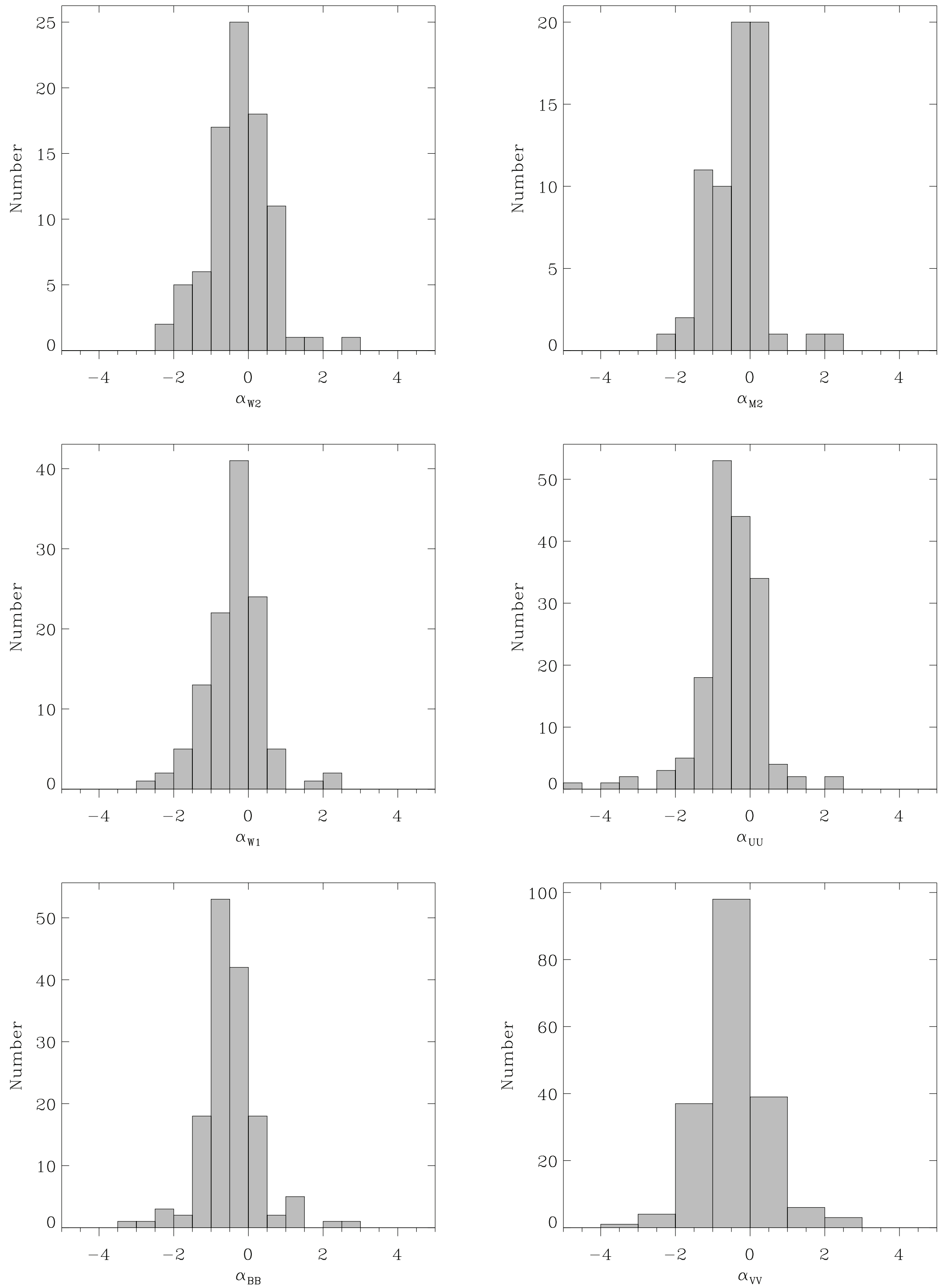

Figure 3. Histogram of the temporal slopes (α) for the first segment of the light curves in each UVOT color filter. Any extreme outliers are not shown in the histogram.

Table 10. General properties of the spectral slopes at fixed epochs

Sample	Epoch	$\overline{\beta}$	β_{Md}	σ	Num	β_{min}	β_{max}
Platinum	2E3	-0.79	-0.70	1.31	82	-2.99	1.97
	2E4	-0.42	-0.50	1.34	80	-2.90	2.75
	2E5	-0.63	-0.76	1.47	81	-2.93	2.81
Gold	2E3	-0.82	-0.71	1.57	91	-3.31	3.48
	2E4	-0.65	-0.53	1.50	87	-3.45	2.75
	2E5	-0.55	-0.72	1.65	86	-3.38	3.43
Silver	2E3	-0.95	-0.98	1.75	98	-3.98	3.86
	2E4	-0.66	-0.56	1.70	92	-3.85	3.89
	2E5	-0.60	-0.76	1.84	92	-3.99	3.66
Bronze	2E3	-1.25	-1.09	2.70	115	-11.28	5.40
	2E4	-1.27	-0.84	3.30	106	-20.72	7.92
	2E5	-1.12	-1.15	3.31	110	-19.79	9.00

NOTE—The sample selection for platinum, gold, silver, and bronze is described in Section 5. The columns are epoch, average ($\overline{\beta}$), median (β_{Md}), standard deviation (σ), number (Num), minimum (β_{min}), and maximum (β_{max}) of the spectral slopes in the sample.

then a shallow decay in the third, changing to another steep decay, and finally a more gentle decay. Morphology "f" starts with a rapid and steep decay, then a rise to peak (in some instances with a break in between the rise), a steep decay, and a final less-steep decay (probably as a result of poor background subtraction due to the background host signal dominating over the GRB signal). We caution that sparsely populated lightcurves tend to be classified as morphological type "d," which may or may not be the actual morphology. Therefore, the percentages quoted here should not be considered representative of the global burst population.

We also examined the relationship between peak afterglow brightness and number of breaks. We find that for light curves with one, two, three, or four segments that the magnitude range (number of GRBs) is 13.73-20.62 (165), 11.43-19.10 (65), 11.41-18.78 (17), and 14.94-15.53 (2), respectively; the mean is 17.93, 16.23, 15.81, and 15.24, respectively. If we take the dimmest magnitude of the four segment sample (15.53) to be the discriminator between bright and dim, we find that 3%, 29%, 35%, and 100% of GRBs are bright for one, two, three, and four segments, respectively. These numbers are not surprising since brighter bursts will have smaller error bars and therefore distinguishing breaks will be much easier. This implies that these values should be taken as lower limits for the distribution of brightness versus numbers of breaks, i.e. the number of bursts with breaks is most likely higher than determined here.

Using the fluxes at 2×10^3, 2×10^4, and 2×10^5 seconds in each UVOT filter, the spectral slopes are calculated. The sample is then culled using only those slopes with $0.01 \le \chi^2_{Red} \le 5$ (e.g. values with $\chi^2_{Red} = 0$, or only two data points, are not included). The culled sample is then divided into a platinum, gold, silver, and bronze sample depending on the degrees-of-freedom (DoF) associated with the χ^2_{Red} and range of β values. For platinum, DoF ≥ 3 and $-3 < \beta < 3$; gold, DoF ≥ 2 and $-3.5 < \beta < 3.5$; silver, DoF ≥ 1 and $-4 < \beta < 4$; and bronze, all DoF ≥ 1. The distribution of the culled spectral slopes are found in Figure 5 and the mean ($\overline{\beta}$), median (β_{Md}), standard deviation (σ), number in the sample (Num), minimum (β_{min}), and maximum (β_{max}) of the spectral slopes at 2×10^3 s, 2×10^4 s, and 2×10^5 s are provided in Table 10.

Figures 6 — 8 show the relationship between the spectral slopes at 2×10^3 s (β_{2E3}), 2×10^4 s (β_{2E4}), and 2×10^5 s (β_{2E5}) for the platinum sample. Using the Spearman rank correlation ($\rho = 0.48$, 0.61, and 0.01, for β_{2E3} versus β_{2E4}, β_{2E4} versus β_{2E5}, and β_{2E3} versus β_{2E5}, respectively), the data are strongly ($P = 7.9 \times 10^{-5}$), strongly ($P < 1 \times 10^{-5}$), and weakly ($P = 0.97$) correlated, respectively. Linear fits to the data are provided in Table 11.

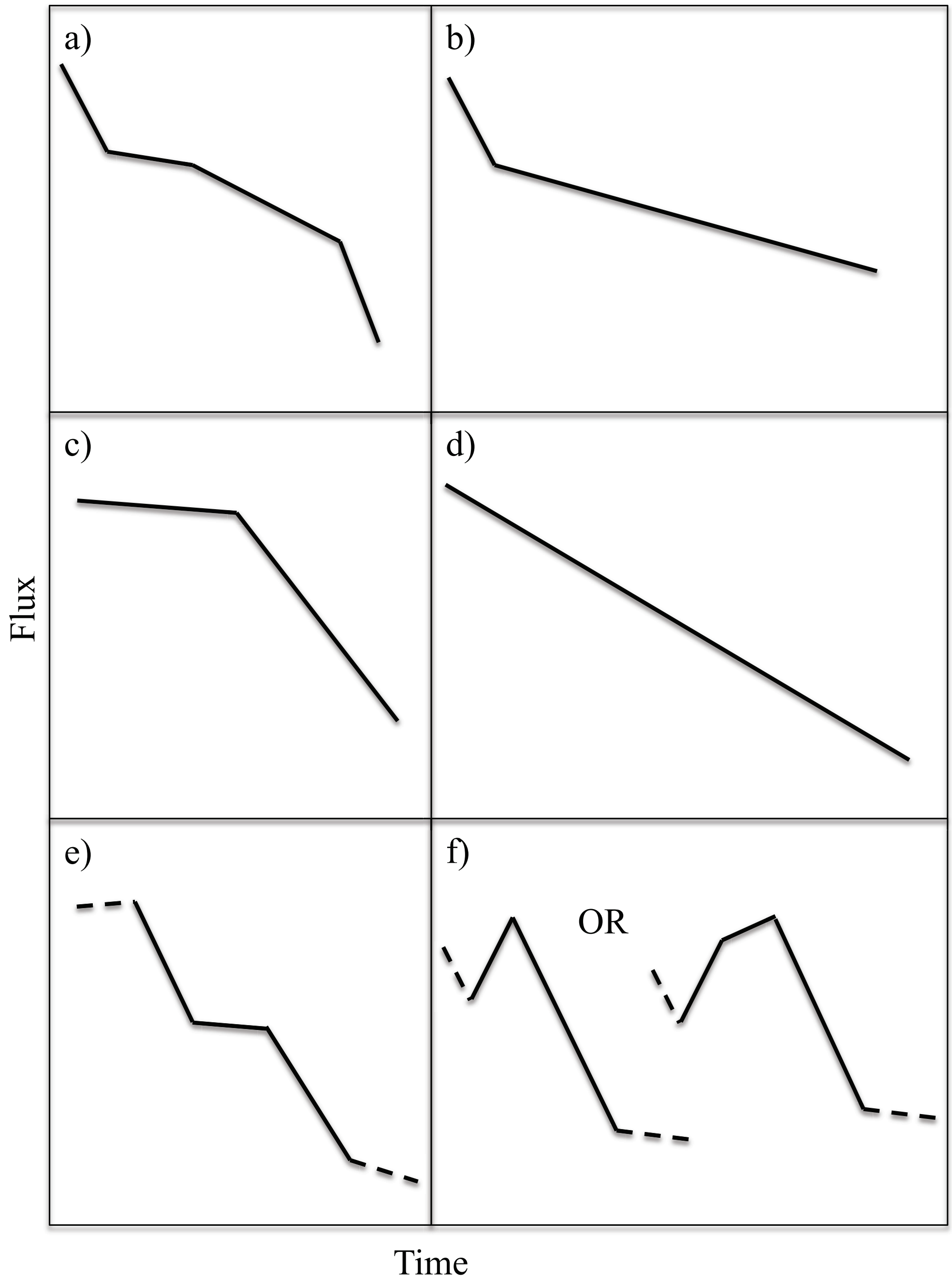

Figure 4. Schematics of GRB lightcurve morphologies adapted from Evans et al. (2009). Morphologies a-d are unchanged from Evans et al. (2009), but morphologies e-f are new. These additional morphologies are representative of some UVOT observed GRBs. Dotted lines represent those portions of the lightcurves that are not always seen in these morphologies.

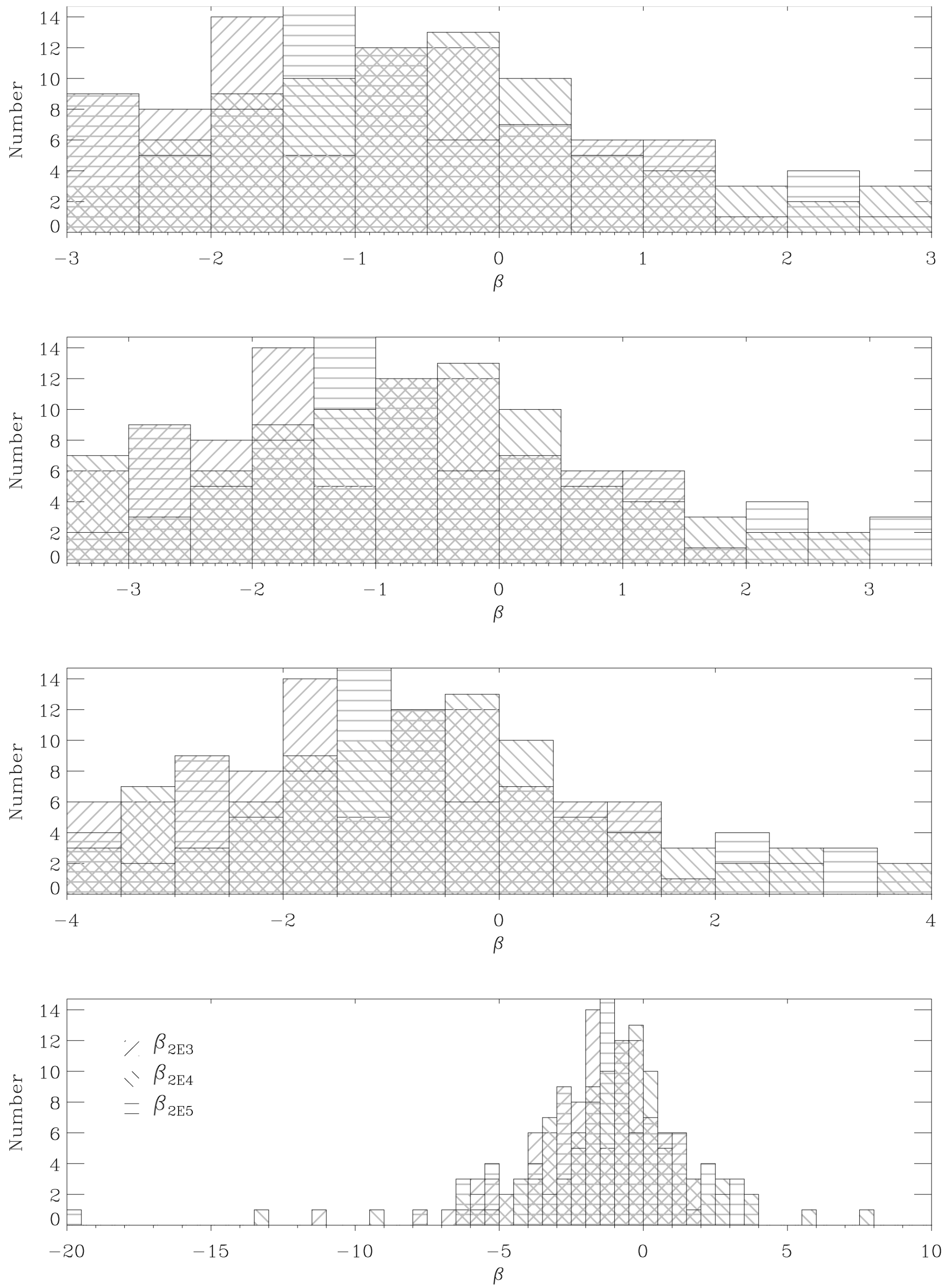

Figure 5. Histogram of the spectral slopes for 2×10^3 s (β_{2E3}), 2×10^4 s (β_{2E4}), and 2×10^5 s (β_{2E5}) for the platinum, gold, silver, and bronze samples.

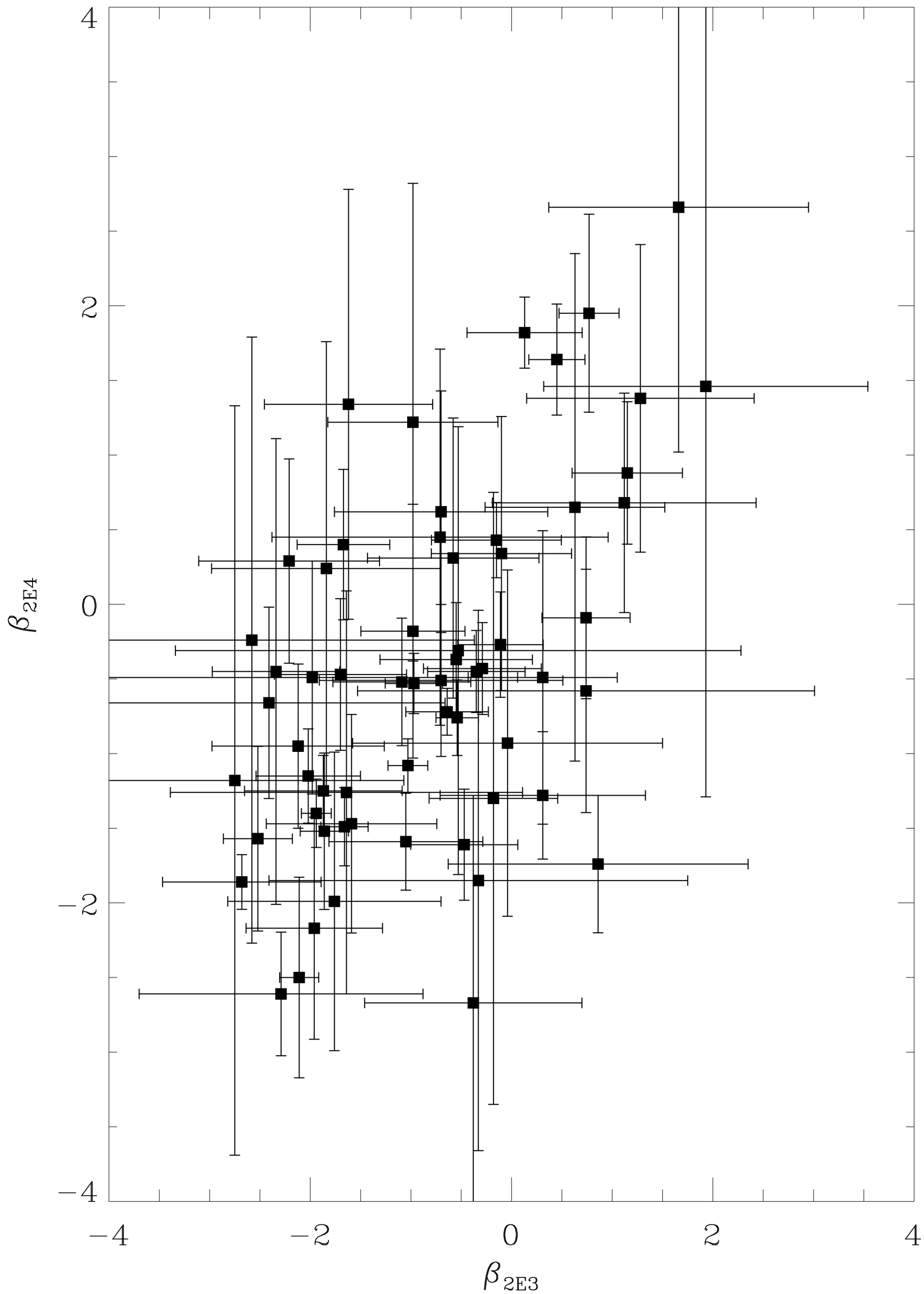

Figure 6. Relationship between the platinum spectral slopes at 2×10^3 s (β_{2E3}) and 2×10^4 s (β_{2E4}). Using the Spearman rank correlation ($\rho = 0.48$), the data are strongly correlated ($P = 7.9 \times 10^{-5}$).

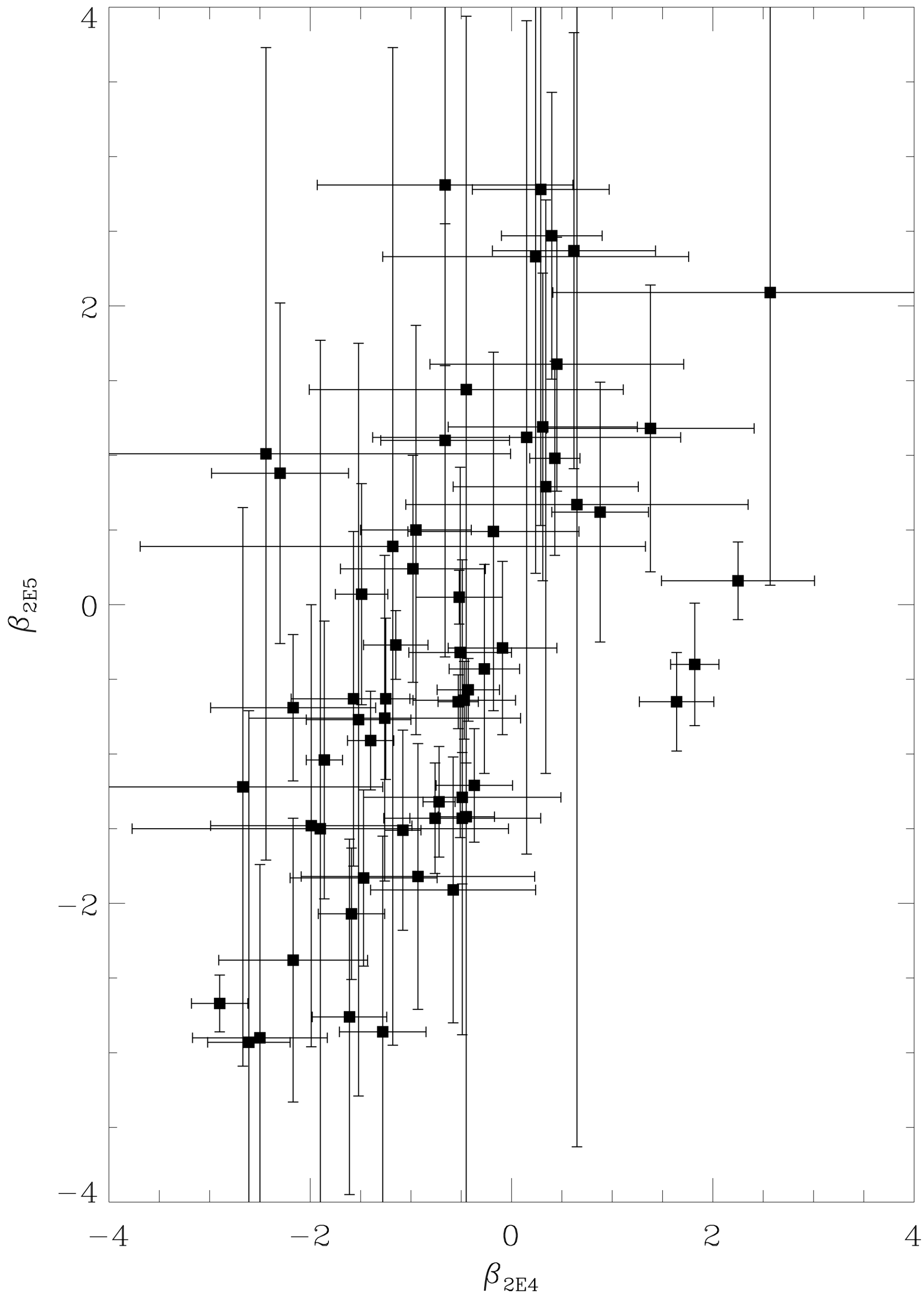

Figure 7. Relationship between the platinum spectral slopes at 2×10^4 s (β_{2E4}) and 2×10^5 s (β_{2E5}). Using the Spearman rank correlation ($\rho = 0.61$), the data are strongly correlated ($P < 1 \times 10^{-5}$).

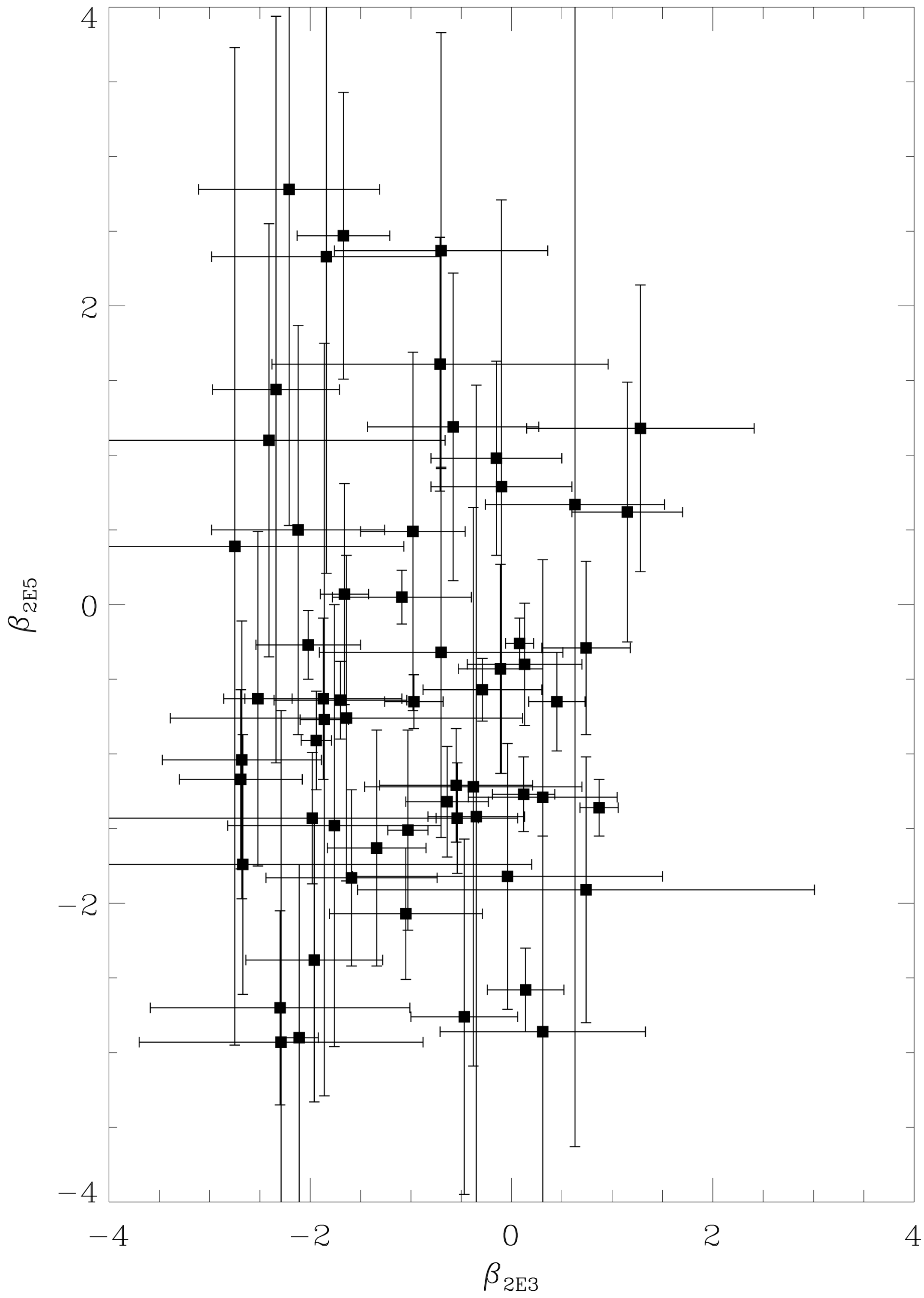

Figure 8. Relationship between the platinum spectral slopes at 2×10^3 s (β_{2E3}) and 2×10^5 s (β_{2E5}). Using the Spearman rank correlation ($\rho = 0.01$), the data are weakly correlated ($P = 0.97$).

Table 11. Fits to correlated data

Data (Figure #)	Equation	x-range	y-range	R^2
β_{2E3} vs. β_{2E4} (6)	$y = 0.53x - 0.02$	-2.75—1.93	-2.67—2.66	0.285
β_{2E4} vs. β_{2E5} (7)	$y = 0.63x + 0.09$	-2.75—1.28	-2.93—2.78	0.000
β_{2E3} vs. β_{2E5} (8)	$y = -0.01x - 0.59$	-2.90—2.75	-2.93—2.81	0.300
β_{XRT} vs. β_{2E3} (9-*Top*)	$y = 1.05x - 3.00$	1.33—3.52	-2.75—2.76	0.093
β_{XRT} vs. β_{2E4} (9-*Middle*)	$y = 0.83x - 2.24$	1.68—3.52	-2.67—2.57	0.044
β_{XRT} vs. β_{2E5} (9-*Bottom*)	$y = 0.40x - 1.41$	1.33—3.52	-2.93—2.81	0.004
Γ_{BAT} vs. β_{2E3} (10-*Top*)	$y = -0.36x - 0.33$	0.70—3.08	-2.75—2.76	0.018
Γ_{BAT} vs. β_{2E4} (10-*Middle*)	$y = 0.38x - 1.21$	0.43—3.08	-2.67—2.75	0.018
Γ_{BAT} vs. β_{2E5} (10-*Bottom*)	$y = 0.44x - 1.57$	0.31—3.08	-2.93—1.61	0.029
T_{90} vs. S_γ (11)	$y = 2.00\text{E-}07x^{0.58}$	0.04—2100.00	6.00E-09—1.05E-04	0.474
$F_{X,e}$ vs. S_γ (12)	$y = 1.00E - 04x^{0.22}$	2.30E-14—6.12E+02	6.00E-09—1.05E-04	0.241
$F_{X,e}$ vs. $F_{U,1}$ (13)	$y = 4.00\text{E-}15x^{0.16}$	2.80E-14—6.12E+02	6.71E-19—1.02E-13	0.060
$F_{U,1}$ vs. S_γ (14)	$y = 0.01x^{0.24}$	2.78E-20—1.02E-13	9.00E-09—1.05E-04	0.102

A comparison of the XRT spectral index (β_{XRT}) to β_{2E3}, β_{2E4}, and β_{2E5} are illustrated in Figure 9. Using the Spearman rank correlation ($\rho = 0.04$, 0.11, and 0.01, respectively), the data are weakly correlated ($P = 0.75$, 0.38, and 0.94, respectively). Linear fits to the data are provided in Table 11. A comparison of the BAT photon index (Γ_{BAT}) to β_{2E3}, β_{2E4}, and β_{2E5} for the platinum sample are illustrated in Figure 10. Again, using the Spearman rank correlation ($\rho = 0.13$, 0.14, and 0.19, respectively), the data are weakly correlated ($P = 0.32$, 0.29, and 0.11, respectively). Linear fits to the data are also provided in Table 11.

Other correlations provided in this paper include: T_{90} versus S_γ (Figure 11), $F_{X,e}$ versus S_γ (Figure 12), $F_{X,e}$ versus the first UVOT flux ($F_{U,1}$; Figure 13), and $F_{U,1}$ versus S_γ (Figure 14). Using the Spearman rank correlation ($\rho = 0.64$, 0.57, 0.18, and 0.27, respectively), the data are shown to be strongly correlated ($P \leq 1 \times 10^{-5}$), with the exception of $F_{X,e}$ to $F_{U,1}$, which is only marginally correlated ($P = 0.02$). The data reveal that longer bursts tend to be of a higher fluence. $F_{X,e}$ and $F_{U,1}$ trend toward larger values with the increase of S_γ, consistent with the results of Gehrels et al. (2008). We note that the data have not been redshift corrected, nor is the UV/optical data at a common epoch or in a common filter.

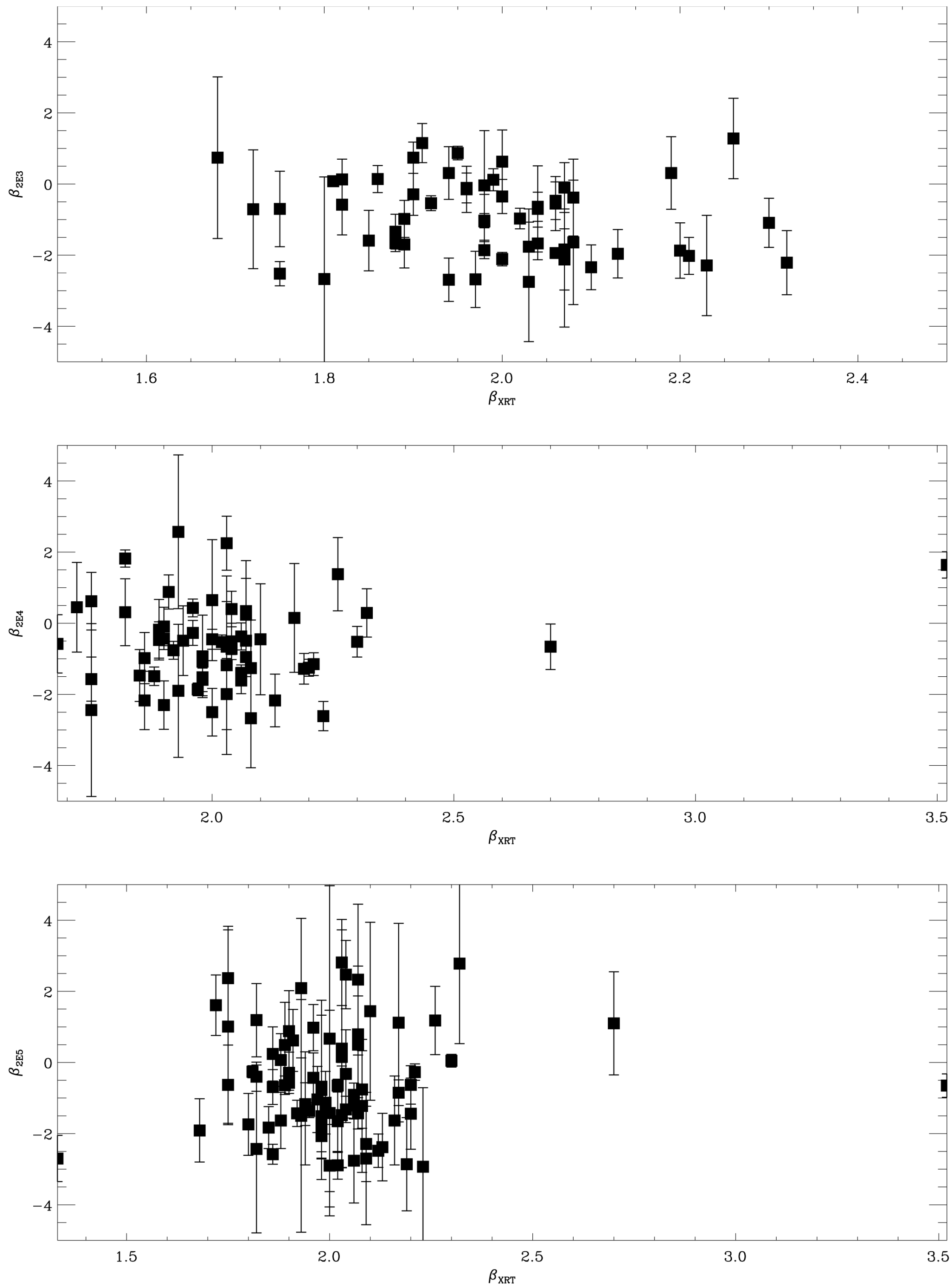

Figure 9. Relationship between the XRT spectral index (β_{XRT}) and the UVOT platinum spectral slopes at 2×10^3 s (β_{2E3}; *Top Panel*), 2×10^4 s (β_{2E4}; *Middle Panel*), and 2×10^5 s (β_{2E5}; *Bottom Panel*). Using the Spearman rank correlation ($\rho =$ 0.04, 0.11, and 0.01, respectively), the data are weakly correlated ($P = 0.75$, 0.38, and 0.94, respectively). Errors in the XRT spectral index are not provided by the SGA and are therefore not provided here.

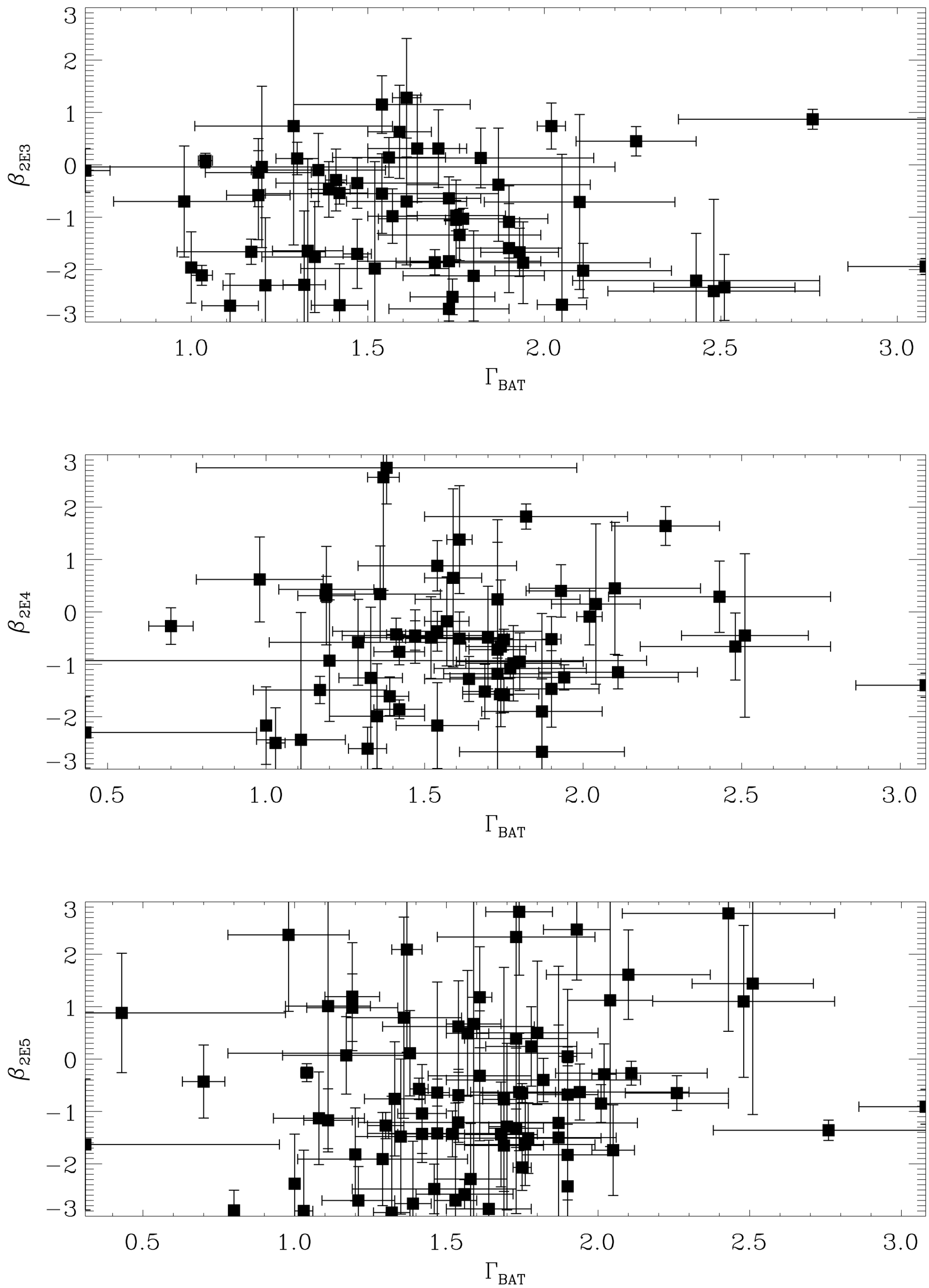

Figure 10. Relationship between the BAT photon index (Γ_{BAT}) and the UVOT platinum spectral slopes at 2×10^3 s (β_{2E3}; *Top Panel*), 2×10^4 s (β_{2E4}; *Middle Panel*), and 2×10^5 s (β_{2E5}; *Bottom Panel*). Using the Spearman rank correlation ($\rho =$ 0.13, 0.14, and 0.19, respectively), the data are weakly correlated ($P = 0.32$, 0.29, and 0.11, respectively).

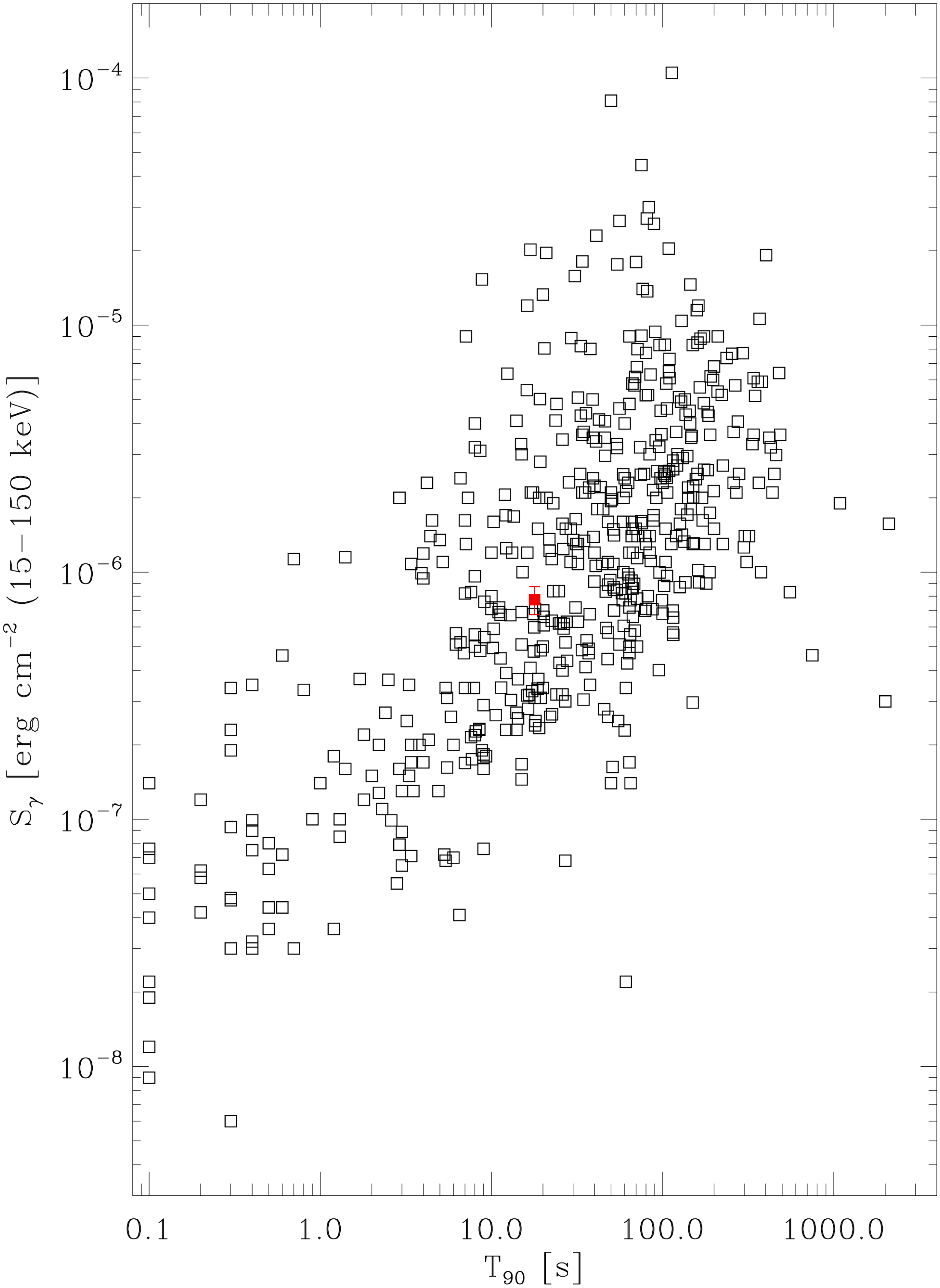

Figure 11. Relationship between T_{90} (in s) and the BAT 15-150 keV fluence (S_γ in $\mathrm{erg\,cm^{-2}}$). Using the Spearman rank correlation ($\rho = 0.64$), the data are shown to be strongly correlated ($P < 1 \times 10^{-5}$). The data have not been corrected for redshift. For clarity, only the median error for S_γ (which is 1.09×10^{-7}) is shown, and is represented by the closed red box (at x-position = 17.89 and y-position = 7.75×10^{-7}) with error bars. Errors on T_{90} are not provided by the SGA and are therefore not provided here. [*See the electronic edition of the Journal for a color version of this figure.*]

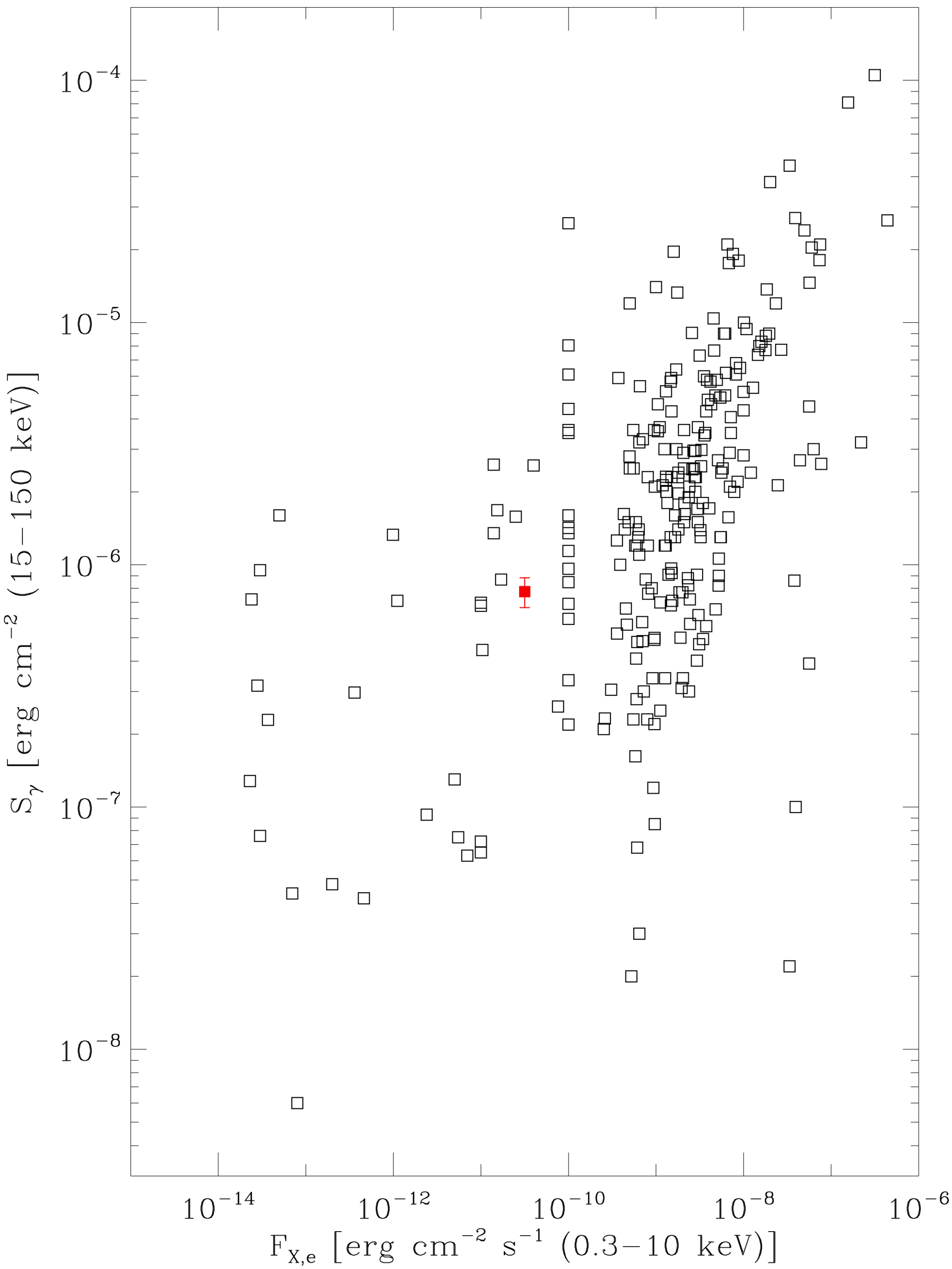

Figure 12. Relationship between the early (first) XRT 0.3-10 keV flux ($F_{X,e}$ in $\mathrm{erg\,cm^{-2}\,s^{-1}}$) and the BAT 15-150 keV fluence (S_γ in $\mathrm{erg\,cm^{-2}}$). Using the Spearman rank correlation ($\rho = 0.57$), the data are shown to be strongly correlated ($P < 1 \times 10^{-5}$). The data have not been corrected for redshift. For clarity, only the median error for S_γ (which is 1.09×10^{-7}) is shown, and is represented by the closed red box (at x-position $= 3.16 \times 10^{-11}$ and y-position $= 7.75 \times 10^{-7}$) with error bars. Errors on $F_{X,e}$ are not provided by the SGA and are therefore not provided here. [*See the electronic edition of the Journal for a color version of this figure.*]

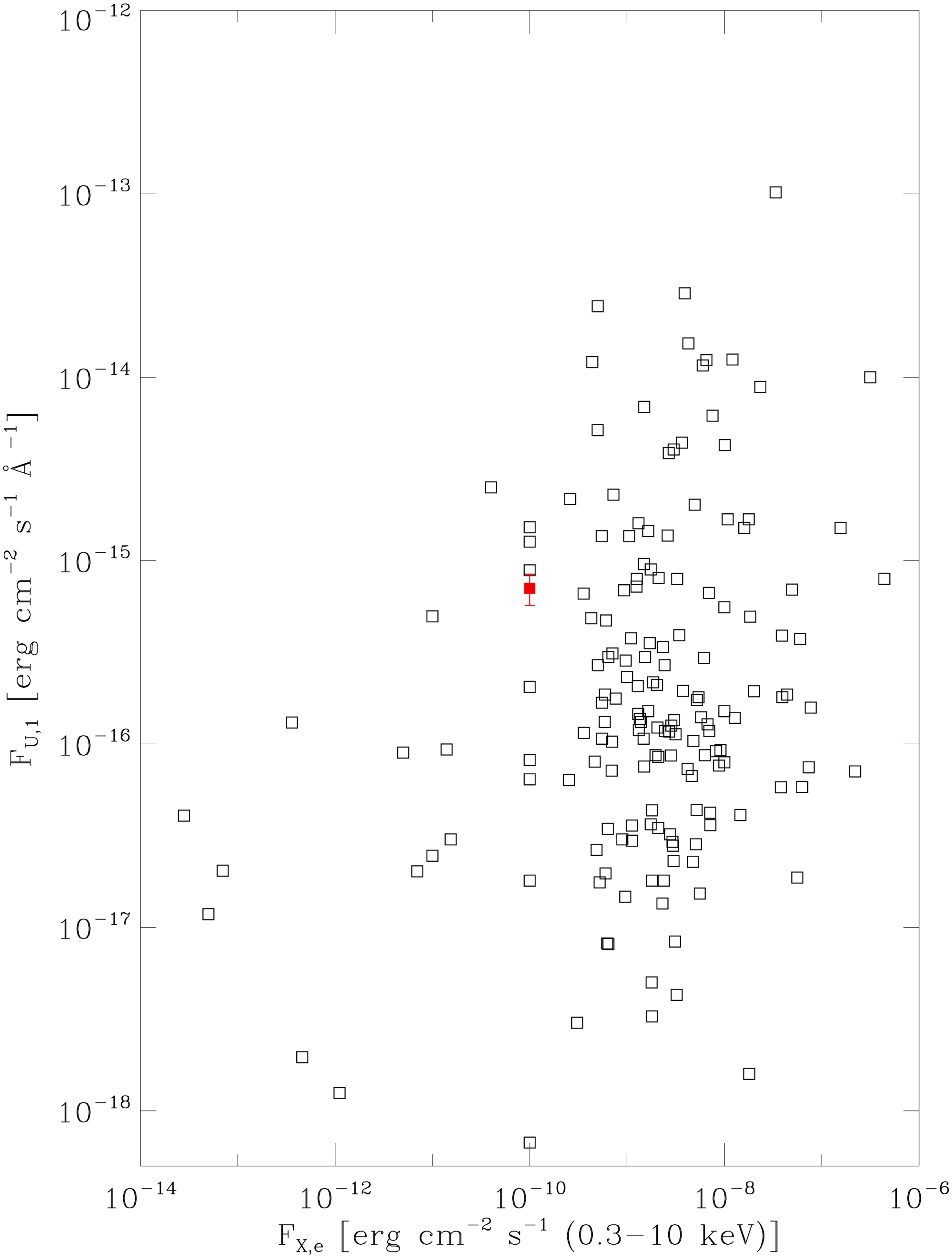

Figure 13. Relationship between the early (first) XRT 0.3-10 keV flux ($F_{X,e}$ in erg cm^{-2} s^{-1}) and the first UVOT flux ($F_{U,1}$ in erg cm^{-2} s^{-1} Å^{-1}). Using the Spearman rank correlation ($\rho = 0.18$), the data are shown to be marginally correlated ($P = 0.02$). The data have not been corrected for redshift, nor is there a common epoch or filter used for the UV/optical data. For clarity, only the median error for $F_{U,1}$ (which is 1.37×10^{-16}) is shown, and is represented by the closed red box (at x-position = 1.00×10^{-10} and y-position = 7.07×10^{-16}) with error bars. Errors on $F_{X,e}$ are not provided by the SGA and are therefore not provided here. [*See the electronic edition of the Journal for a color version of this figure.*]

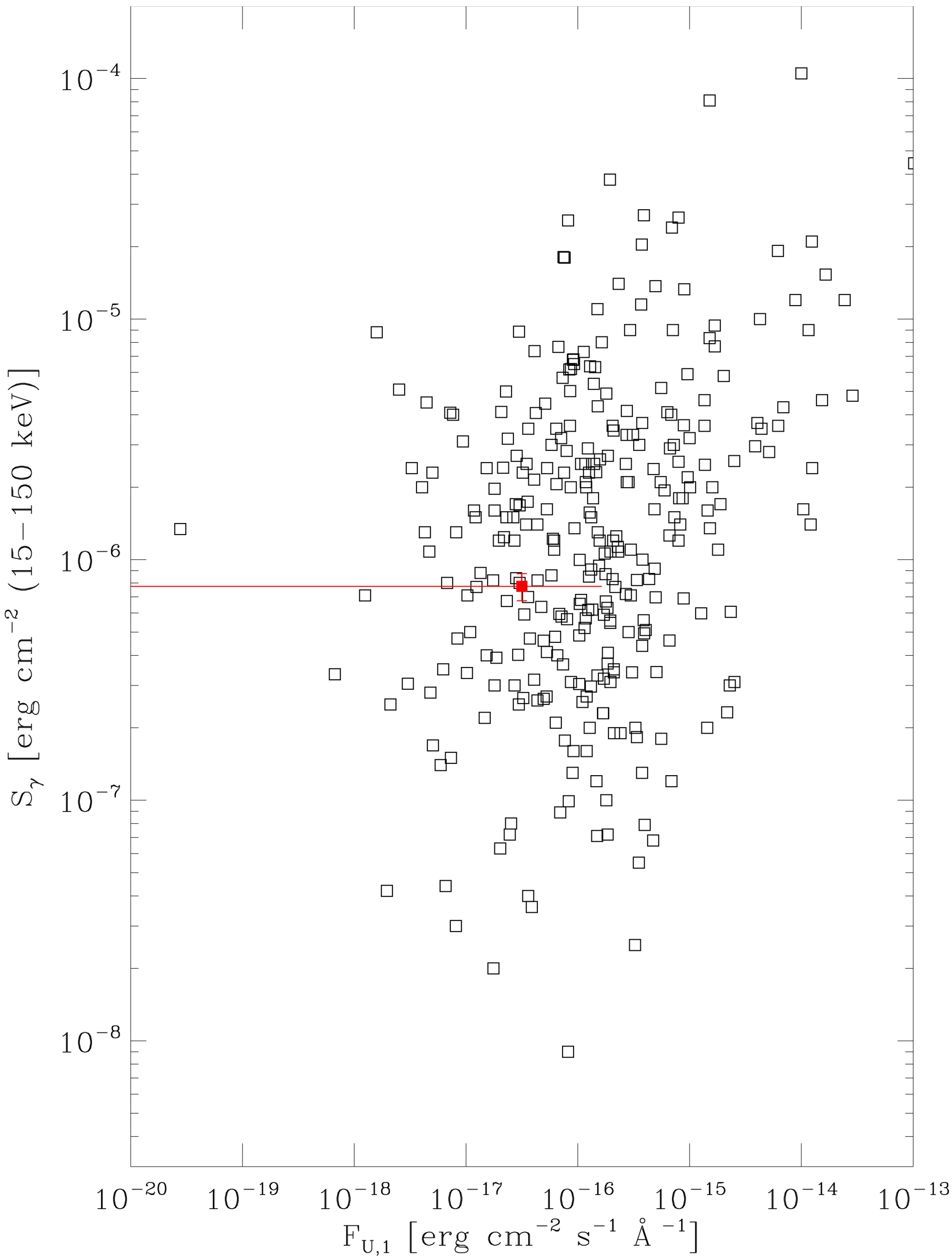

Figure 14. Relationship between the first UVOT flux ($F_{U,1}$ in erg cm^{-2} s^{-1} Å^{-1}) and the BAT 15-150 keV fluence (S_γ in erg cm^{-2}). Using the Spearman rank correlation ($\rho = 0.27$), the data are shown to be strongly correlated ($P = 1 \times 10^{-5}$). The data have not been corrected for redshift, nor is there a common epoch or filter used for the UV/optical data. For clarity, only the median errors for $F_{U,1}$ (which is 1.37×10^{-16}) and S_γ (which is 1.09×10^{-7}) are shown, and is represented by the closed red box (at x-position = 5.00×10^{-16} and y-position = 7.75×10^{-7}) with error bars. [*See the electronic edition of the Journal for a color version of this figure.*]

6. CONCLUSIONS AND FUTURE WORK

In this paper we describe the second *Swift* UVOT GRB afterglow catalog and its corresponding databases. This catalog significantly expands upon the first *Swift* UVOT GRB afterglow catalog (Paper1) and provides spectral information that was not available in Paper1. The detection rate in this current catalog has increased due to the use of optimal coaddition (M08). Due to the significantly larger amount of data available in this version of the catalog, we were able to refine the temporal slopes per UVOT filter for multiple light curve segments and to include average break times per filter.

From the temporal slopes and break times, we were able to compare our morphological results with that in the X-ray (Evans et al. 2009). We find that $\sim 75\%$ of the UVOT light curves have one of the four morphologies identified by Evans et al. (2009). The remaining $\sim 25\%$ have a newly identified morphology, which we designate as morphology type "e" and "f," continuing where Evans et al. (2009) left off. Although many of the bursts were classified as morphological type "d," we did not remove poorly sampled light curves from our database, thus many type-d's may be misclassified. Future work includes breaking up the database into "gold," "silver," and "bronze" light curves in order to more accurately determine the UV/optical morphological distribution of the global burst population.

We also examined the spectral slopes at fixed epochs (2×10^3 s, 2×10^4 s, and 2×10^5 s). The spectral slopes were divided into a platinum, gold, silver, and bronze sample. Using the platinum sample, we find that there is a strong correlation between the early-mid and mid-late time spectral slopes, while the early-late spectral slopes were only weakly correlated. Future efforts include targeting specific epochs with a larger number of data points in each individual burst which will further increase the accuracy of the spectral slopes. Coupling time-dependent UV/optical and X-ray spectral slopes would be a powerful tool for probing the environments of massive stars (i.e. windy or ISM) and would help determine the fraction of GRBs with their cooling break (ν_b) between the optical and X-ray. Time-dependent UV/optical and X-ray temporal and spectral slopes would also help validate and further constrain GRB afterglow models (cf. Zhang & Mészáros 2004; Zhang et al. 2006).

We are grateful to Jeff Kommers for input into this paper which greatly strengthened this work. We gratefully acknowledge the contributions from members of the *Swift* team at the Pennsylvania State University (PSU), University College London/Mullard Space Science Laboratory (MSSL), NASA/Goddard Space Flight Center, and our subcontractors, who helped make the UVOT possible. This work is supported under NASA grant number NNX13AF26G, at PSU by NASA contract NAS5-00136, and at MSSL by funding from the United Kingdom Space Agency (UKSA).

Facility: Facilities: Swift(UVOT)

REFERENCES

Atwood, W. B., et al. 2009, ApJ, 697, 1071

Barthelmy, S. D., Butterworth, P., Cline, T. L., Gehrels, N., Fishman, G. J., Kouveliotou, C., & Meegan, C. A. 1995, Ap&SS, 231, 235

Barthelmy, S. D., Butterworth, P., Cline, T. L., & Gehrels, N. 1998, in AIP Conf. Proc. 428, 4th Huntsville Symp. on Gamma-Ray Bursts, ed. C. A. Meegan, R. D. Preece, & T. M. Koshut (New York: AIP), 139

Barthelmy, S. D., et al. 2005, SSRv, 120, 143

Blustin, A. J., et al. 2006, ApJ, 637, 901

Burrows, D. N., et al. 2005, SSRv, 120, 165

Butler, N. R. 2007, AJ, 133, 1027

Cardelli, J. A., Clayton, G. C., & Mathis, J. S. 1989, ApJ, 345, 245

D'Elia, V., & Stratta, G. 2012, Mem. S. A. It. Suppl., 21, 22

De Pasquale, M., et al. 2007, MNRAS, 377, 1638

De Pasquale, M., et al. 2010, ApJ, 709, L146

Evans, P. A., et al. 2009, MNRAS, 397, 1177

Fynbo, J. U., et al. 2009, ApJS, 185, 526

Gehrels, N., et al. 2004, ApJ, 611, 1005

Gehrels, N., et al. 2008, ApJ, 689, 1161

Goad, M., et al. 2007, A&A, 476, 1401

Goad, M., et al. 2008, A&A, 492, 873

Gordon, K. D., Cartledge, S., & Clayton, G. C. 2009, ApJ, 705, 1320

Gordon, K. D., Cartledge, S., & Clayton, G. C. 2014, ApJ, 781, 128

Grupe, D., et al. 2006, ApJ, 645, 464

Grupe, D., et al. 2007, ApJ, 662, 443

Hurley, K., et al. 2005, ApJS, 156, 217

Jeong, S., et al. 2014, A&A, 569, A93

Kouveliotou, C., et al. 1993, ApJ, 413, L101

Kuin, N. P. M., & Rosen, S. R. 2008, MNRAS, 383, 383

Kuin, N. P. M., et al. 2009, MNRAS, 395, L21

Markwardt, C. B. 2009, in ASP Conf. Ser. 411, Astronomical Data Analysis Software and Systems XVIII ed. D. A. Bohlender, D. Durand, & P. Dowler (San Francisco: ASP), 251

Morgan, A. N., et al. 2008, ApJ, 683, 913 (M08)

Nousek, J. A., et al. 2006, ApJ, 642, 389

Oates, S. R., et al. 2007, MNRAS, 380, 270

Oates, S. R., et al. 2009, MNRAS, 395, 490

Page, K. L., et al. 2009, MNRAS, 400, 134

Page, M. J., et al. 2013, MNRAS, 436, 1684

Pandey, S. B., et al. 2010, ApJ, 714, 799

Pei, Y. C. 1992, ApJ, 395, 130

Perri, M., et al. 2007, A&A, 471, 83

Poole, T. S., et al. 2008, MNRAS, 383, 627

Racusin, J. L., et al. 2008, Nature, 455, 183

Racusin, J. L., et al. 2009, ApJ, 698, 43

Ricker, G. R. 1997, in All-Sky X-Ray Observations in the Next Decade, ed. M. Matsuoka & N. Kawai (Japan: RIKEN), 366

Romano, P., et al. 2006, A&A, 456, 917

Roming, P. W. A., et al. 2000, Proc. SPIE, 4140, 76

Roming, P. W. A., et al. 2004, Proc. SPIE, 5165, 262

Roming, P. W. A., et al. 2005, SSRv, 120, 95

Roming, P. W. A., et al. 2006, ApJ, 651, 985

Roming, P. W. A., et al. 2006, ApJ, 652, 1416

Roming, P. W. A., et al. 2009, ApJ, 690, 163 (Paper1)

Sakamoto, T., et al. 2008, ApJS, 175, 179

Sakamoto, T., et al. 2011, ApJS, 195, 2

Schady, P., et al. 2007, MNRAS, 380, 1041

Schady, P., et al. 2010, MNRAS, 401, 2773

Schady, P., et al. 2012, A&A, 537, A15

Schlafly, E. F., & Finkbeiner, D. P. 2011, ApJ, 737, 103

Tavani, M., et al. 2009, A&A, 502, 995

Updike, A. C., et al. 2008, ApJ, 685, 361

Xin, L. -P., et al. 2011, MNRAS, 410, 27

Yuan, F., et al. 2010, ApJ, 711, 870

Zhang, B., & Mészáros, P. 2004, Int. J. Mod. Phys. A, 19, 2385

Zhang, B., Fan, Y. Z., Dyks, J., Kobayashi, S., Mészáros, P., Burrows, D. N., Nousek, J. A., & Gehrels, N. 2006, ApJ, 642, 354